

A BCool survey of the magnetic fields of planet-hosting solar-type stars

M. W. Mengel,^{1*} S. C. Marsden,¹ B. D. Carter,¹ J. Horner,¹ R. King,¹
 R. Fares,² S. V. Jeffers,³ P. Petit,^{4,5} A. A. Vidotto,⁶ J. Morin,⁷
 and the BCool Collaboration

¹Computational Engineering and Science Research Centre, University of Southern Queensland, Toowoomba, Qld, Australia

²INAF - Osservatorio Astrofisico di Catania, Via Santa Sofia, 78, I-95123 Catania, Italy

³Institut für Astrophysik, Georg-August-Universität Göttingen, Friedrich-Hund-Platz 1, 37077 Göttingen, Germany

⁴Université de Toulouse, UPS-OMP, Institut de Recherche en Astrophysique et Planétologie, F-31400 Toulouse, France

⁵CNRS, Institut de Recherche en Astrophysique et Planétologie, 14 Avenue Edouard Belin, F-31400 Toulouse, France

⁶School of Physics, Trinity College Dublin, The University of Dublin, Dublin 2, Ireland

⁷Laboratoire Univers et Particules de Montpellier, Université de Montpellier, CNRS, place Eugène Bataillon, F-34095 Montpellier, France

Accepted 2016 November 11. Received 2016 November 10; in original form 2016 September 29

ABSTRACT

We present a spectropolarimetric snapshot survey of solar-type planet hosting stars. In addition to 14 planet-hosting stars observed as part of the BCool magnetic snapshot survey, we obtained magnetic observations of a further 19 planet-hosting solar-type stars in order to see if the presence of close-in planets had an effect on the measured surface magnetic field ($|B_{\ell}|$). Our results indicate that the magnetic activity of this sample is congruent with that of the overall BCool sample. The effects of the planetary systems on the magnetic activity of the parent star, if any, are too subtle to detect compared to the intrinsic dispersion and correlations with rotation, age and stellar activity proxies in our sample. Four of the 19 newly observed stars, two of which are subgiants, have unambiguously detected magnetic fields and are future targets for Zeeman Doppler Mapping.

Key words: line: profiles - stars: activity - stars: magnetic fields - techniques: polarimetric - planetary systems.

1 INTRODUCTION

1.1 The BCool Spectropolarimetric Survey

The BCool spectropolarimetric survey (Marsden et al. 2014) has the objective of observing a large sample of solar-type stars with $V \lesssim 9$, attempting to detect their magnetic fields. This serves a two-fold purpose. First, the survey sets out to determine if there is any correlation between the large-scale stellar magnetic field and various stellar parameters. Secondly, the characterisation of the magnetic fields of the targeted stars allows for the selection of optimal or interesting targets for further study, such as long-term monitoring and mapping of their magnetic field topology in order to observe and characterise their magnetic cycles.

Marsden et al. (2014) published spectropolarimetric snapshots of 170 solar-type stars, and reported that the strength of the large-scale magnetic field declines as a func-

tion of age and with reduced rotation. Additionally, they found that the mean surface magnetic field detected was higher for K-dwarfs compared to G-dwarfs and F-dwarfs. Marsden et al. (2014) do note this higher field for K dwarfs may be due to selection biases, although this observation would also be consistent with even stronger fields seen on M dwarfs (e.g. Morin et al. 2008). At the most fundamental level, this work adds 19 additional solar-type stars to the BCool sample.

In this work, we also aim to examine whether the presence of a planetary system or the nature of the planets in that system correlates with the large-scale magnetic field of the host star. Such correlation would potentially be indicative of star-planet interaction (SPI).

1.2 Star-Planet Interaction

Host stars profoundly influence their surrounding planetary environment. The transfer of angular momentum, stellar winds and magnetic fields play roles in planetary formation,

* E-mail: matthew.mengel@usq.edu.au (MWM)

migration and evolution (Horner & Jones 2010). Additionally, stellar winds in cool stars, which are influenced by the variation in stellar magnetic fields, affect the planetary environment and can interact strongly with planetary atmospheres (See et al. 2015; Strugarek et al. 2015; Vidotto et al. 2015). Understanding the magnetic field of host stars allows us to more fully investigate and understand the planetary environment around them, and by extension, examine the habitability of potential Earth-like planets.

Tidal and magnetic interaction between host stars and their planets, especially large close-in “hot Jupiters”, has been of considerable interest since the discovery of such planets. Whether such companions result in any change in the magnetic activity of the star remains unanswered. Cuntz et al. (2000), Rubenstein & Schaefer (2000) and Lanza (2009, 2012) variously suggest that close-in planets may spin up the host star by transfer of angular momentum resulting in higher activity. Activity enhancement may also occur due to magnetic reconnection events between stellar and planetary magnetic fields. Evidence for star-planet interaction has been claimed for several stars using a variety of observed phenomena synchronised with the orbital period of the planet, such as photospheric “hot spots” (Lanza et al. 2011), chromospheric enhancement (Shkolnik et al. 2005, 2008), and X-ray enhancement (Pillitteri et al. 2010).

A statistical assessment of SPI by Miller et al. (2015) shows that no particular correlation exists between proxies for SPI strength and coronal activity. A relationship with solar type (FGK) stars was found, however they note that this is only driven by a handful of extreme hot Jupiter systems. Miller et al. (2015) also investigated whether planetary properties were correlated with UV luminosity or Ca II H&K and found no significant difference between hot Jupiter systems and others. This was in contrast to the conclusions drawn from earlier observations by Shkolnik (2013) and Krejčová & Budaj (2012). However, all such studies note that selection effects may skew these results.

Finally, France et al. (2016) presents tentative evidence for SPI for close-in, massive planets via an enhancement of the transition region. France et al. (2016) speculate that this may be due to magnetospheric interaction, but urge caution due to a small sample size.

2 TARGET SELECTION

2.1 New Targets (Not Previously Observed by BCool)

Targets were chosen from the exoplanet.eu database¹ (Schneider et al. 2011). The host stars of the planetary systems were chosen to be broadly solar-type with T_{eff} between 5100 K and 6300 K and $M_{\star} < 1.5M_{\odot}$, on the main sequence or at the subgiant stage. This selection was further constrained by the observational requirements of the NARVAL instrument and the T el escope Bernard Lyot (see Sec. 3.1). Targets were chosen with magnitude $V \lesssim 9$ and declination δ above -10° .

Table 1 shows the configurations of the observed planetary systems. There are six stars which host a planet that

can be classified as a hot Jupiter (considering the definition of a massive planet with a semi-major axis of less than ~ 0.05 au). Further, three systems contain two or more detected planets.

The stellar parameters of the host stars are shown in Table 2. 12 of the 19 targets were included in the SPOCS (Valenti & Fischer 2005) database, and thus their parameters were taken from Valenti & Fischer (2005) and Takeda et al. (2007). For the remaining targets, the stellar parameters were sourced from the references listed in the table. Figure 1 shows the stars in our sample on a Hertzsprung-Russell (HR) diagram superimposed on the stars for the BCool sample (Marsden et al. 2014, Fig. 1). Figure 1 shows that the sample stars in this work are similar in general characteristics to the full BCool sample. Three of the stars in our sample are classified as sub-giants with the remainder being dwarf stars.

The lower panel of Figure 1 shows the rotation velocity ($v \sin i$) for our sample against effective temperature, also superimposed on the overall BCool sample. As shown, the sample exhibits a decrease in rotation rate with decreasing effective temperature. Our entire sample of planet-hosting stars display $v \sin i < 10 \text{ km s}^{-1}$, which we note is at the lower end of the BCool sample.

2.2 The BCool Sample

In addition to the survey described above, we extracted the 14 known planet-hosting stars from the BCool sample. As the methods used to derive their various parameters are the same as this new work, we did not re-analyse the data. Instead, we use the results from Marsden et al. (2014) in our Discussion and Conclusions. The planetary and stellar parameters are shown in Appendix B, as are the magnetic and chromospheric results from Marsden et al. (2014) for these stars.

3 OBSERVATIONS AND DATA PROCESSING

3.1 Instrument and Observational Procedure

Observations were obtained using the polarimetric mode of the NARVAL spectropolarimeter (attached to the T el escope Bernard Lyot located at Observatoire du Pic du Midi). NARVAL is composed of a bench mounted high resolution spectrograph and a Cassegrain-mounted polarimetry module. The spectrograph has an optical wavelength coverage of 370 to 1000 nm, and a resolution of ~ 65000 with a pixel size of 2.6 km s^{-1} .

The polarimetric module performs polarimetry over the entire spectral range using a series of three Fresnel rhombs. The light is then split into two beams containing opposite polarisation states. These two beams are fed via individual fibres to the spectrograph, allowing the simultaneous capture of both polarisation states and further allowing the unpolarised Stokes I and circularly-polarised Stokes V spectra to be determined from each observation. Further information on NARVAL can be found in Auri ere (2003).

Each Stokes V observation consists of a sequence of four individual exposures. Effectively, this results in eight individual spectra; four left-hand and four right-hand circularly

¹ <http://exoplanet.eu>

Table 1. Planetary parameters of the sample of planet-hosting solar type stars not previously observed by Marsden et al. (2014). The stellar component’s *Hipparcos* number, SPOCS catalogue number and HD number (where applicable) are shown in the first three columns. Column 4 refers to the Name by which the planetary components (column 5) are known. The period, projected mass ($M \sin i$) and semi-major axis are shown for each planet. These values are taken from the references listed in the last column; locations where values were unavailable in the literature are denoted by ‘X’. Parameters for the systems observed by the BCool survey are shown in Table B1.

Star			Planet(s)					
HIP no.	SPOCS no.	HD no.	Name	Component	Period (d)	$M \sin i$ (M_J)	Semi-major axis (au)	Refs.
14954	155	19994	94 Cet	b	537.7 ± 3.1	1.69 ± 0.26	1.428 ± 0.083	1
17747	184	23596	HD 23596	b	1565 ± 21	7.8 ± 1.1	2.83 ± 0.17	1
24205 ⁺	252	33636	HD 33636	b	2127.7 ± 8.2	9.28 ± 0.77	3.37 ± 0.19	1
25191		290327	HD 290327	b	2443^{+205}_{-117}	$2.54^{+0.17}_{-0.14}$	$3.43^{+0.20}_{-0.12}$	2
26381	270	37124	HD 37124	b	$154.46 \pm X$	0.64 ± 0.11	0.529 ± 0.031	1
			HD 37124	c*	$2295.00 \pm X$	0.683 ± 0.088	3.19 ± 0.18	1
			HD 37124	d	$843.60 \pm X$	0.624 ± 0.063	1.639 ± 0.095	1
26664		37605	HD 37605	b	54.23 ± 0.23	2.86 ± 0.41	0.261 ± 0.015	1
27253	282	38529	HD 38529	b	14.3093 ± 0.0013	0.852 ± 0.074	0.1313 ± 0.0076	1
			HD 38529	c	2165 ± 14	13.2 ± 1.1	3.74 ± 0.22	1
27384		38801	HD 38801	b	696.3 ± 2.7	10.7 ± 0.5	1.70 ± 0.03	3
28767	293	40979	HD 40979	b	263.84 ± 0.71	3.83 ± 0.36	0.855 ± 0.049	1
29301		42176	KELT2A	b	4.11379 ± 0.00001	1.524 ± 0.088	0.05504 ± 0.00086	4
30057		43691	HD 43691	b	36.96 ± 0.02	$2.49 \pm X$	$0.24 \pm X$	5
32916	324	49674	HD 49674	b	4.94737 ± 0.00098	0.105 ± 0.011	0.0580 ± 0.0034	1
45406		79498	HD 79498	b	1966.1 ± 41	1.34 ± 0.07	3.13 ± 0.08	6
64457	556	114783	HD 114783	b	496.9 ± 2.3	1.034 ± 0.089	1.169 ± 0.068	1
95740	841	183263	HD 183263	b	635.4 ± 3.9	3.82 ± 0.4	1.525 ± 0.088	1
96507		185269	HD 185269	b	6.8399 ± 0.0013	1.03 ± 0.03	$0.077 \pm X$	7
98767	870	190360	HD 190360	b	2891 ± 85	1.55 ± 0.14	3.99 ± 0.25	1
			HD 190360	c	17.100 ± 0.015	0.0587 ± 0.0078	0.1303 ± 0.0075	1
101966	901	196885	HD 196885	b	1326.0 ± 3.7	2.98 ± 0.05	2.6 ± 0.1	8
108859	953	209458	HD 209458	b	$3.52474554 \pm 1.8 \times 10^{-7}$	0.689 ± 0.057	0.0474 ± 0.0027	1

References: 1: Butler et al. (2006), 2: Naef et al. (2010), 3: Harakawa et al. (2010), 4: Beatty et al. (2012), 5: da Silva et al. (2007), 6: Robertson et al. (2012), 7: Moutou et al. (2006), 8: Chauvin et al. (2011).

⁺ - HIP 24205 (HD 33636) at the time of writing is listed in some catalogues of planet-hosting stars, however Martioli et al. (2010) have determined the mass of the companion to be much too massive to be considered a planet. While perhaps considered no longer planet-hosting, in the interests of completeness we include it in our analysis.

* - Butler et al. (2006) indicates that the mass of HD 37124 c is unclear and an alternative interpretation is for a period of 29.3 d, $M \sin i = 0.170 M_J$ and semi-major axis of 0.170 au, with slightly different values for HD 37124 a and HD 37124 b.

polarised. As described by Petit et al. (2003), the polarisation states in the fibre pair described above are alternated during the sequence to help eliminate instrumental effects; the first and fourth exposures have one arrangement of polarisation states whilst the second and third have the opposite arrangement. Adding all eight spectra yields the unpolarised Stokes I (intensity) spectrum. The polarised Stokes V spectrum is obtained as per Donati et al. (1997, Eqs. 1, 2):

$$\frac{V}{I} = \frac{R_V - 1}{R_V + 1} \quad (1)$$

where

$$R_V^4 = \frac{i_{1,\perp}/i_{1,\parallel}}{i_{2,\perp}/i_{2,\parallel}} \frac{i_{4,\perp}/i_{4,\parallel}}{i_{3,\perp}/i_{3,\parallel}} \quad (2)$$

and $i_{k,\perp}$ and $i_{k,\parallel}$ are the two polarised spectra in each exposure, k .

By destructively adding the spectra, a null polarisation spectrum, N , can be obtained (Donati et al. 1997, Eqs. 1, 3):

$$\frac{N}{I} = \frac{R_N - 1}{R_N + 1} \quad (3)$$

where

$$R_N^4 = \frac{i_{1,\perp}/i_{1,\parallel}}{i_{4,\perp}/i_{4,\parallel}} \frac{i_{2,\perp}/i_{2,\parallel}}{i_{3,\perp}/i_{3,\parallel}} \quad (4)$$

As described in Bagnulo et al. (2009), a significant signal (i.e. deviation from zero) in the N spectrum may be indicative of a spurious polarisation signal.

Table 2. Stellar parameters of the sample of planet-hosting solar type stars not previously observed by Marsden et al. (2014). The spectral type is taken from SIMBAD (<http://simbad.u-strasbg.fr/simbad/>, Wenger et al. (2000)). Column 11 is the radius of the convective zone of the star. Values are found in the references shown in the final column of the table; locations where values were unavailable in the literature are denoted by ‘X’. ^{SG} indicates the star is a subgiant (see Fig. 1). Parameters for the systems observed by the BCool survey are shown in Table B2.

HIP no.	SPOCS no.	Spec. Type	T_{eff} (K)	$\log(g)$ (cm s^{-2})	[M/H] or [Fe/H] (*)	$\log(\text{Lum})$ (L_{\odot})	Age (Gyr)	Mass (M_{\odot})	Radius (R_{\odot})	Radius _{CZ} (R_{\odot})	$v \sin i$ (km s^{-1})	Refs.
14954	155	F8.5V	6188 ⁺⁴⁴ ₋₄₄	4.17 ^{+0.03} _{-0.08}	+0.17 ^{+0.03} _{-0.03}	+0.574 ^{+0.035} _{-0.035}	2.56 ^{+0.40} _{-0.36}	1.365 ^{+0.042} _{-0.024}	1.75 ^{+0.06} _{-0.16}	0.265 ^{+0.009} _{-0.009}	8.6 ^{+0.5} _{-0.5}	1, 2
17747	184	F8	5904 ⁺⁴⁴ ₋₄₄	4.07 ^{+0.04} _{-0.04}	+0.24 ^{+0.03} _{-0.03}	+0.446 ^{+0.089} _{-0.089}	5.68 ^{+0.48} _{-0.36}	1.159 ^{+0.062} _{-0.018}	1.69 ^{+0.09} _{-0.08}	0.472 ^{+0.035} _{-0.030}	4.2 ^{+0.5} _{-0.5}	1, 2
24205	252	G0	5904 ⁺⁴⁴ ₋₄₄	4.44 ^{+0.04} _{-0.04}	-0.12 ^{+0.03} _{-0.03}	+0.039 ^{+0.077} _{-0.077}	3.52 ^{+2.16} _{-2.44}	1.017 ^{+0.032} _{-0.032}	1.02 ^{+0.04} _{-0.04}	0.247 ^{+0.020} _{-0.015}	3.1 ^{+0.5} _{-0.5}	1, 2
25191		G0	5552 ⁺²¹ ₋₄₄	4.42 ^{+0.04} _{-0.04}	* -0.11 ^{+0.02} _{-0.02}	-0.143 ^{+X} _{-X}	> 3	0.90 ^{+X} _{-X}	1.00 ^{+0.01} _{-0.01}	X	1.4 ^{+1.0} _{-1.0}	10
26381	270	G4IV-V	5500 ⁺⁴⁴ ₋₄₄	4.44 ^{+0.04} _{-0.02}	-0.29 ^{+0.03} _{-0.03}	-0.077 ^{+0.077} _{-0.077}	11.7 ^{+3.1} _{-8.4}	0.850 ^{+0.022} _{-0.016}	0.93 ^{+0.03} _{-0.04}	0.277 ^{+0.011} _{-0.018}	1.2 ^{+0.5} _{-0.5}	1, 2
26664 ^{SC}		K0	5448 ⁺⁴⁴ ₋₄₄	4.51 ^{+0.02} _{-0.02}	* +0.34 ^{+0.03} _{-0.03}	+0.590 ^{+0.058} _{-0.058}	7.07 ^{+X} _{-X}	1.000 ^{+0.050} _{-0.050}	0.90 ^{+0.05} _{-0.05}	X	< 1	3, 4
27253 ^{SC}	282	G8III/IV	5697 ⁺⁴⁴ ₋₄₄	3.94 ^{+0.02} _{-0.02}	+0.27 ^{+0.03} _{-0.03}	+0.802 ^{+0.079} _{-0.079}	3.28 ^{+0.36} _{-0.24}	1.477 ^{+0.040} _{-0.052}	2.50 ^{+0.08} _{-0.06}	0.711 ^{+0.031} _{-0.014}	3.9 ^{+0.5} _{-0.5}	1, 2
27384 ^{SC}		G8IV	5222 ⁺⁴⁴ ₋₄₄	3.84 ^{+0.10} _{-0.10}	* +0.26 ^{+0.03} _{-0.03}	+0.659 ^{+0.043} _{-0.047}	4.67 ^{+2.56} _{-2.56}	1.36 ^{+0.09} _{-0.09}	2.53 ^{+0.13} _{-0.13}	X	0.5 ^{+0.5} _{-0.5}	5
28767	293	F8	6089 ⁺⁴⁴ ₋₄₄	4.32 ^{+0.04} _{-0.03}	+0.12 ^{+0.03} _{-0.03}	+0.257 ^{+0.055} _{-0.055}	3.56 ^{+0.68} _{-0.80}	1.154 ^{+0.028} _{-0.022}	1.23 ^{+0.05} _{-0.04}	0.273 ^{+0.020} _{-0.018}	7.4 ^{+0.5} _{-0.5}	1, 2
29301		F7V	6148 ⁺⁴⁸ ₋₄₈	4.03 ^{+0.02} _{-0.03}	* +0.03 ^{+0.08} _{-0.08}	+0.550 ^{+X} _{-X}	3.97 ^{+0.01} _{-0.01}	1.314 ^{+0.063} _{-0.060}	1.84 ^{+0.07} _{-0.05}	X	9.0 ^{+2.0} _{-2.0}	11, 13
30057		G0	6200 ⁺⁴⁰ ₋₄₀	4.28 ^{+0.13} _{-0.13}	* +0.28 ^{+0.05} _{-0.05}	+0.521 ^{+X} _{-X}	2.8 ^{+0.8} _{-0.8}	1.38 ^{+0.05} _{-0.05}	X	X	4.7 ^{+X} _{-X}	6, 13
32916	324	G0	5662 ⁺⁴⁴ ₋₄₄	4.51 ^{+0.03} _{-0.03}	+0.22 ^{+0.03} _{-0.03}	-0.089 ^{+0.094} _{-0.094}	X	1.015 ^{+0.048} _{-0.036}	0.95 ^{+0.04} _{-0.04}	0.271 ^{+0.013} _{-0.009}	0.4 ^{+0.5} _{-0.5}	1, 2
45406		G5	5760 ⁺⁸⁰ ₋₈₀	4.37 ^{+0.12} _{-0.12}	* +0.24 ^{+0.06} _{-0.06}	X	2.70 ^{+X} _{-X}	1.06 ^{+X} _{-X}	X	X	X	7, 8
64457	556	K1V	5135 ⁺⁴⁴ ₋₄₄	4.57 ^{+0.03} _{-0.04}	+0.10 ^{+0.03} _{-0.03}	-0.415 ^{+0.045} _{-0.045}	6.76 ^{+X} _{-X}	0.853 ^{+0.034} _{-0.038}	0.81 ^{+0.02} _{-0.03}	0.255 ^{+0.020} _{-0.010}	0.9 ^{+0.5} _{-0.5}	1, 2
95740	841	G2IV	5936 ⁺⁴⁴ ₋₄₄	4.36 ^{+0.05} _{-0.05}	+0.22 ^{+0.03} _{-0.03}	+0.210 ^{+0.110} _{-0.110}	4.52 ^{+0.76} _{-1.12}	1.121 ^{+0.064} _{-0.040}	1.18 ^{+0.07} _{-0.07}	0.304 ^{+0.026} _{-0.023}	1.6 ^{+0.5} _{-0.5}	1, 2
96507		G2V	6059 ⁺¹⁸ ₋₁₈	4.13 ^{+0.06} _{-0.06}	* +0.12 ^{+0.02} _{-0.02}	+0.49 ^{+0.1} _{-0.1}	3.4 ^{+0.54} _{-0.54}	1.33 ^{+0.07} _{-0.07}	1.76 ^{+0.07} _{-0.07}	X	5.5 ^{+X} _{-X}	9, 12
98767	870	G7IV-V	5552 ⁺⁴⁴ ₋₄₄	4.31 ^{+0.03} _{-0.02}	+0.19 ^{+0.03} _{-0.03}	+0.050 ^{+0.022} _{-0.022}	13.4 ^{+X} _{-1.84}	0.983 ^{+0.026} _{-0.048}	1.15 ^{+0.03} _{-0.03}	0.397 ^{+0.008} _{-0.022}	2.2 ^{+0.5} _{-0.5}	1, 2
101966	901	F8IV	6185 ⁺⁴⁴ ₋₄₄	4.26 ^{+0.03} _{-0.03}	+0.13 ^{+0.03} _{-0.03}	+0.383 ^{+0.054} _{-0.054}	3.12 ^{+0.36} _{-0.4}	1.230 ^{+0.028} _{-0.020}	1.38 ^{+0.06} _{-0.05}	0.270 ^{+0.020} _{-0.019}	7.7 ^{+0.5} _{-0.5}	1, 2
108859	953	G0V	6099 ⁺⁴⁴ ₋₄₄	4.39 ^{+0.04} _{-0.04}	+0.02 ^{+0.03} _{-0.03}	+0.197 ^{+0.095} _{-0.095}	2.44 ^{+1.32} _{-1.64}	1.131 ^{+0.026} _{-0.024}	1.14 ^{+0.05} _{-0.05}	0.241 ^{+0.018} _{-0.016}	4.5 ^{+0.5} _{-0.5}	1, 2

References: 1: Valenti & Fischer (2005), 2: Takeda et al. (2007), 3: Wang et al. (2012), 4: Isaacson & Fischer (2010), 5: Harakawa et al. (2010), 6: da Silva et al. (2007), 7: Casagrande et al. (2011), 8: Robertson et al. (2012), 9: Moutou et al. (2006), 10: Naef et al. (2010), 11: Beatty et al. (2012), 12: Jofré et al. (2015), 13: McDonald et al. (2012).

3.2 Spectropolarimetric Observations

All observations were made using NARVAL at Télescope Bernard Lyot between September 2014 and January 2015. Each star was observed once, except for HIP 64457, which was observed twice. Each observation consisted of a spectropolarimetric sequence of four 900s exposures. The journal of observations is shown in Table 3.

3.3 Data Processing

Observations were automatically reduced by a pipeline process utilising the LIBRE-ESPRIT package. LIBRE-ESPRIT is based on the ESPRIT software (Donati et al. 1997). The reduced Stokes *I* and Stokes *V* spectra were produced using 1.8 km s⁻¹ pixel resolution.

3.4 Least Squares Deconvolution

Zeeman signatures are typically very small and usually the S/N in a reduced spectrum is insufficient for a detection in a single line (Donati et al. 1992). Least Squares Deconvolution (LSD) is a multiline technique which extracts Stokes *I* and Stokes *V* information from each individual spectral line in the reduced spectrum and determines an average profile with a higher S/N than for each individual line (Donati et al. 1992; Kochukhov et al. 2010).

Marsden et al. (2014) computed a set of line masks for use in LSD for the BCool sample using the Vienna Atomic

Table 3. Journal of Observations showing the object, date and time of the observation, and the exposure time used. As explained in Sec. 3.1, a Stokes *V* observation consists of a sequence of four exposures, hence the nomenclature used here.

HIP no.	HJD 2450000+	Date	UT hh:mm:ss	T_{exp} (s)
14954	7033.33090	2015-01-10	19:53:06	4 × 900
17747	6958.50071	2014-10-27	23:53:43	4 × 900
24205	6926.67026	2014-09-26	04:02:50	4 × 900
25191	7034.43181	2015-01-11	22:15:20	4 × 900
26381	6957.55553	2014-10-27	01:14:29	4 × 900
26664	6962.64066	2014-11-01	03:17:03	4 × 900
27253	6982.58476	2014-11-21	01:55:21	4 × 900
27384	6960.64135	2014-10-30	03:19:08	4 × 900
28767	6927.68776	2014-09-27	04:27:50	4 × 900
29301	6994.63288	2014-12-03	03:04:50	4 × 900
30057	6994.71807	2014-12-03	05:08:10	4 × 900
32916	6959.64396	2014-10-29	03:23:27	4 × 900
45406	6995.69091	2014-12-04	04:31:58	4 × 900
64457	7030.70798	2015-01-08	04:59:21	4 × 900
	7032.69851	2015-01-10	04:45:26	4 × 900
95740	6995.28708	2014-12-03	18:58:48	4 × 900
96507	6982.30247	2014-11-20	19:18:19	4 × 900
98767	6982.35222	2014-11-20	20:29:11	4 × 900
101966	6984.27534	2014-11-22	18:38:31	4 × 900
108859	6957.33207	2014-10-26	19:53:29	4 × 900

Line Database (VALD²; Kupka et al. 2000). These masks are

² <http://vald.astro.unive.ac.at/~vald/php/vald.php>

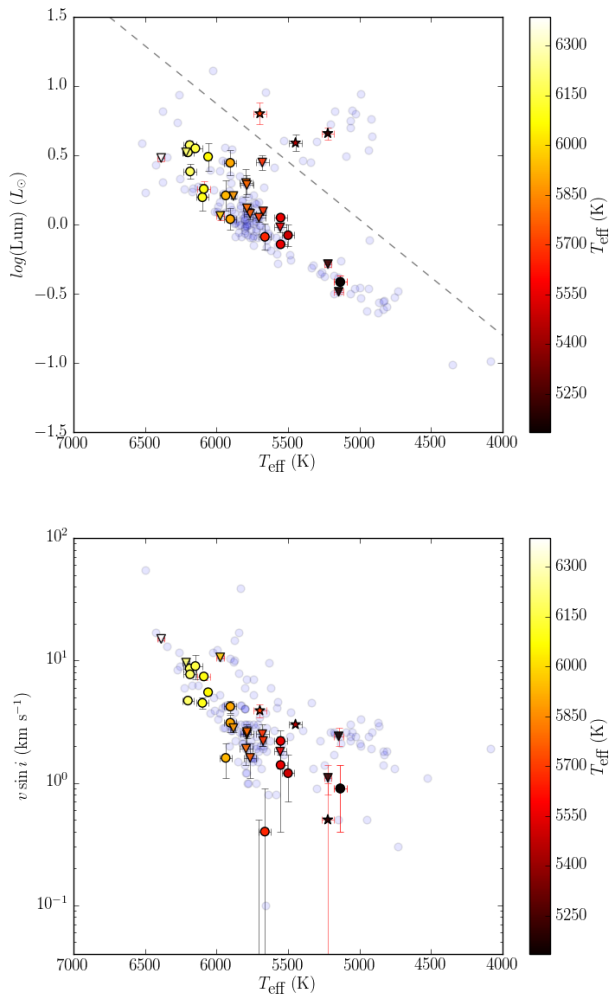


Figure 1. HR diagram (upper panel) and $v \sin i$ vs T_{eff} plot (lower panel) for the survey stars (Table 2; circular and star-shaped points) overlaid on the entire BCool sample (blue circles, data from Marsden et al. (2014, Fig. 1)). Planet-hosting stars from the BCool survey (Table B2) are shown as inverted triangles. Points with red error bars are magnetic detections, and the colour of the data points represents the effective temperature. Five-pointed star-shaped data points indicate sub-giants and circles represent dwarfs with the dashed line dividing these two categories (note inverted triangles from the BCool survey are all dwarfs; no planet-hosts in the BCool sample were subgiants). This dashed dividing line is in the same position as Marsden et al. (2014, Fig. 1).

derived from stellar atmospheric and spectral synthesis models using the stellar parameters T_{eff} , $\log(g)$ and $\log(M/H)$ (or $\log(\text{Fe}/H)$ if $\log(M/H)$ is unavailable or unknown). For consistency, these same masks were used in this work, and the range of parameters and step size used is shown in Table 4. For more details on the creation of the set of line masks, see Marsden et al. (2014, Sec. 3.3).

For each target, the appropriate line mask was chosen, and LSD profiles for Stokes I and Stokes V were created with a resolved element of 1.8 km s^{-1} . Depending on the stellar

Table 4. Stellar parameters used to generate line masks for use in LSD. From Marsden et al. (2014, Table 2).

Parameter	Units	Range	Step size
T_{eff}	K	4000 – 6500	250
$\log(g)$	cm s^{-2}	3.5 – 4.5	0.5
$\log(M/H)$		–0.2 to +0.2	0.2

Table 5. Normalization parameters used to produce LSD profiles, following Marsden et al. (2014, Table 4). d_0 = line central depth, λ_0 = line central wavelength, g_0 = line Landé factor

T_{eff} (K)	d_0	λ_0 (nm)	g_0
4000	0.55	650.0	1.22
4250	0.55	640.0	1.22
4500	0.55	630.0	1.22
4750	0.55	620.0	1.22
5000	0.54	610.0	1.22
5250	0.54	600.0	1.22
5500	0.53	590.0	1.22
5750	0.52	580.0	1.22
6000	0.51	570.0	1.22
6250	0.50	570.0	1.21
6500	0.49	560.0	1.21

parameters of the star in our sample, the number of lines used in the LSD process varies from ~ 7000 to ~ 14000 .

As in Marsden et al. (2014), the weighting of the spectral lines was adjusted such that the mean weights of the Stokes V and Stokes I profiles were close to unity. We use the equations given by Marsden et al. (2014, Eqs. 3, 4, 5) for calculating mean weights, and the same normalisation parameters (d_0 = line central depth, λ_0 = line central wavelength, g_0 = line Landé factor), varied for each 250 K step in effective temperature. The normalisation parameters are additionally used in the calculation of the longitudinal magnetic field (Sec. 3.5) and are reproduced in Table 5.

3.5 The Longitudinal Magnetic Field

The mean longitudinal magnetic field, B_ℓ (or given as $\langle B_Z \rangle$ in some publications) is the line-of-sight component of the stellar magnetic field integrated over the visible disc of the star. B_ℓ can be obtained from the Stokes I and Stokes V LSD profiles. From Donati et al. (1997); Mathys (1989), for the given velocity (v , in km s^{-1}) space:

$$B_\ell = -2.14 \times 10^{11} \frac{\int v V(v) dv}{\lambda_0 g_0 c \int [I_c - I(v)] dv} \quad (5)$$

where B_ℓ is in gauss, and λ_0 and g_0 are given in Table 5. c is the speed of light in km s^{-1} and I_c is the continuum level of the Stokes I LSD profile and is normalised to 1. The error in B_ℓ (B_{err}) is calculated by propagating the uncertainties in the reduction pipeline through equation 5. As mentioned by Marsden et al. (2014) and discussed in depth by Shorlin et al. (2002, Sec. 5), the uncertainty depends upon the S/N of the observation, the number of lines used to produce the Stokes V profile, and the depth and width of the average line. The line depth and width scale linearly with $v \sin i$.

An additional uncertainty in B_ℓ is introduced by the choice of the velocity domain used to integrate equation 5.

A narrow velocity domain potentially excludes polarised signals, while a domain which is too wide potentially introduces spurious signals due to the noise in the Stokes V spectrum. For consistency with the measurement of B_ℓ of the BCool sample, the method outlined by Marsden et al. (2014) was used. B_ℓ was calculated using a range of velocity domains, following which, the domain for which the ratio of $|B_\ell|/B_{err}$ was maximised was chosen.

For each observation, the value of B_ℓ was calculated for the null profile (N_ℓ) over the same velocity domain used for the Stokes V profile. A value of $|N_\ell|$ which is close to zero is indicative that the magnetic field measurement is unaffected by spurious polarisation signals. This is indeed the case for the majority of our sample. Where $|N_\ell|$ departs significantly from zero, and is large relative to $|B_\ell|$, the measurement must be considered carefully. The values of B_ℓ and N_ℓ for each observation, and the velocity domain used for the calculations are presented in Table 6.

3.6 Magnetic Detection

Donati et al. (1992) and Donati et al. (1997) describe a method of determining whether a magnetic field is “detected” on a star using the Stokes V profile. That is, a probability is calculated as to whether the variations in the Stokes V LSD profile are likely due to the presence of a magnetic field rather than from noise.

Reduced χ^2 statistics are calculated for the Stokes V and N profiles, inside and outside the spectral lines as defined by the position of the unpolarised Stokes I profile in velocity space. From these values a False Alarm Probability (FAP) is determined. An unambiguous (or definite) detection is defined as having $FAP < 10^{-5}$ (corresponding to a χ^2 probability greater than 99.999 percent). A marginal detection is defined as having $10^{-5} < FAP < 10^{-3}$ (χ^2 probability between 99.999 and 99.9 percent). It is to be noted that there are no marginal detections in our sample. $FAP > 10^{-3}$ is classified as a non-detection.

For each observation, the FAP and the classification as a definite detection (D) or non-detection (N) is shown in Table 6. It should be noted that irrespective of the detection state, values for B_ℓ and N_ℓ are shown. The probability function used to determine the FAP takes into account the Stokes V and N both inside and outside the spectral lines, whereas the values of N_ℓ and B_ℓ are calculated only over a velocity domain containing the spectral lines. Thus detections depend on the false alarm probability rather than absolute longitudinal field values. In general, for non-detections (N), B_ℓ will be of the same order as N_ℓ , i.e. the probability is that the measured B_ℓ is due to noise in the Stokes V LSD profile rather than magnetic activity. The exception in our sample is HIP 28767 (see Table 6 and Appendix A3), which has a value of N_ℓ close to the calculated B_ℓ , but a very low FAP (i.e. similar values of N_ℓ and B_ℓ do not necessarily preclude a detection).

3.7 Radial Velocities

The radial velocities of the host stars of the planetary systems were determined in this work (Table 6) and compared, where available, to those calculated by Nidever et al.

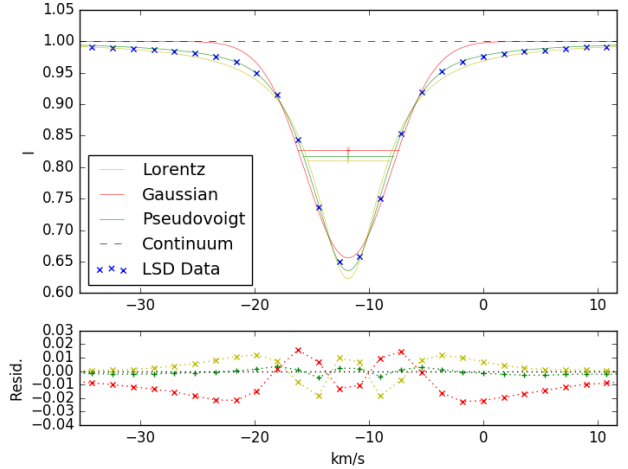


Figure 2. Determining the radial velocity of HIP 64457 (HD 114783). The data from the unpolarised Stokes I LSD profile is shown by the blue crosses. Gaussian (red), Lorentz (yellow) and Pseudovoigt (green) profiles are fitted to the LSD profile data (upper panel). Residuals from each fit are shown in the lower panel. The centroid of the Pseudovoigt fitted profile is taken as the radial velocity of the star.

(2002). A Pseudovoigt profile was fitted to the Stokes I LSD profile of each observation, with the centroid of the Pseudovoigt considered to be the radial velocity (e.g. Fig 2). The long-term radial velocity stability of NARVAL is 30 m s^{-1} (Moutou et al. 2007).

While our values are generally close to those previously published, it must be noted that since our sample stars host planetary systems, there will be intrinsic variation in the radial velocity of the host star due to the gravitational influence of the planets. Thus differences, potentially of significant magnitude, are to be expected depending upon the specific time of observation and the orbital configurations. Hence the values are presented as indicative only, and for completeness with the BCool sample.

3.8 Stellar Activity Proxies

As for the BCool sample, various measures of stellar activity were calculated for each target in our sample. In addition to the Ca II H&K S-index (Wright et al. 2004), Ca II infrared triplet (IRT) and H α indices were derived.

3.8.1 Ca II H & K Emission (S-index)

Following the methodology of Wright et al. (2004), Marsden et al. (2014) determined for NARVAL the coefficients a , b , c , d , and e (see Table 7) of the equation:

$$\text{S-index} = \frac{aF_H + bF_K}{cF_{R_{HK}} + dF_{V_{HK}}} + e \quad (6)$$

where F_H and F_K are the fluxes in 2.18 \AA triangular bandpasses centred on the cores of the Ca II H&K lines and $F_{R_{HK}}$ and $F_{V_{HK}}$ are the fluxes in two rectangular 20 \AA bandpasses

centred on the continuum either side of the HK lines at 3901.07 Å and 4001.07 Å respectively.

For each reduced unpolarised spectrum of each star, overlapping orders were removed. Equation 6 was then applied to the remaining spectrum, generating the Ca II H&K S-indices for each spectrum. As per Marsden et al. (2014), the sample standard deviation of the S-indices for each star was calculated as an empirical measure of the uncertainty. The mean and standard deviation values for each star are shown in Table 8.

3.8.2 Derived Chromospheric Parameters

The S-indices were then used to derive various chromospheric parameters for each star, all of which are shown in Table 8. $\log(R'_{HK})$ was derived using Wright et al. (2004, eqs. 9-12), using *Hipparcos* $B - V$ values. Using the further formulations from Wright et al. (2004, eqs. 13-15), $\log(P_{rot}/\tau)$ (\log (Rossby number)), the chromospheric period and chromospheric age for each target were calculated.

3.8.3 H α Emission

The H α -index was determined for each unpolarised reduced spectrum using the equation:

$$\text{H}\alpha\text{-index} = \frac{F_{H\alpha}}{F_{V_{H\alpha}} + F_{R_{H\alpha}}} \quad (7)$$

where $F_{H\alpha}$ is the flux from a 3.6 Å rectangular bandpass centred on the H α line (6562.85 Å), and $F_{V_{H\alpha}}$ and $F_{R_{H\alpha}}$ are the fluxes in 2.2 Å rectangular bandpasses located on the continuum either side of the H α line centred at 6558.85 and 6567.30 Å. These bandpasses are defined by Gizis et al. (2002, Table 3).

As for the S-index, the sample standard deviation of the H α -indices for each star was calculated as an empirical measure of the uncertainty. The mean and standard deviation of the H α -index for each star are shown in Table 8.

3.8.4 Ca II IRT Emission

The activity index for the Ca II infrared triplet (Ca_{IRT}-index) was calculated from each unpolarised reduced spectrum using the equation (Petit et al. 2013, eq. 1):

$$\text{Ca}_{\text{IRT}}\text{-index} = \frac{F_{8498} + F_{8542} + F_{8662}}{F_{V_{\text{IRT}}} + F_{R_{\text{IRT}}}} \quad (8)$$

where F_{8498} , F_{8542} and F_{8662} are the integrated fluxes of three 2 Å rectangular bandpasses centred on the corresponding Ca II IRT lines (located at 8498.02, 8542.09 and 8662.14 Å), while $F_{V_{\text{IRT}}}$ and $F_{R_{\text{IRT}}}$ are the fluxes in 5 Å rectangular bandpasses located on the continuum either side of the Ca II triplet at 8475.8 and 8704.9 Å. The mean and standard deviation of the Ca_{IRT}-index for each star are shown in Table 8.

4 RESULTS AND DISCUSSION

4.1 Magnetic Detections

Due to the small size of our sample, we did not attempt a comprehensive analysis of detection rates and their correlation with stellar and observational parameters as per (Marsden et al. 2014). However, we can make some broad observations relating to the overall BCool sample.

Of the sample of 19 newly-observed stars, we obtained magnetic detections with a FAP $< 10^{-5}$ on four targets. As noted by Marsden et al. (2014) for the BCool sample in general, the detection rates of the magnetic field drop with increasing age, with decreasing $v \sin i$, and with decreasing activity (i.e. S-index). Given that our sample of planet-hosting stars are generally older than 2 Gyr, are relatively slow rotators, and have low activity indices, it is to be expected that our overall detection rate will be low. As such, it is unsurprising that it is in fact lower than the overall BCool sample. Using the broad categorization of Marsden et al. (2014) (G-stars: $5000 \text{ K} \leq T_{eff} \leq 6000 \text{ K}$; F-Stars: $T_{eff} > 6000 \text{ K}$) we have a 25 percent detection rate for G-stars (cf. 38% BCool) and 14 percent for F-stars (cf. 32% BCool).

Higher measured B_ℓ correlates with a higher S-index, and magnetic detections are more prevalent with higher S-indices ($\gtrsim 0.18$). However, some magnetic detections with lower S-indices are apparent; these exceptions generally have a significantly higher SN_{LSD}. This correlation is also noted by Marsden et al. (2014).

Even if we consider the additional planet-hosting stars from the BCool survey (Appendix B), our detection rate remains very low (24% of the 33 total stars). Our rate is even lower if the two very young planet-hosts HIP 16537 (ϵ Eri; $0.00_{-0.00}^{+0.60}$ Gyr) and HIP 107350 (HN Peg; $0.00_{-0.00}^{+0.88}$ Gyr) from the BCool survey are disregarded as outliers, given that high activity (and thus magnetic field) is strongly correlated with young age and rapid rotation.

We find a correlation with S-index. All stars with an S-index greater than ~ 0.18 obtained a detection. Only one star of our 19 new targets, HIP 27253, with an S-index below 0.18 (0.1750 ± 0.0005) produced a detection. This result is consistent with the finding from Marsden et al. (2014) that, as would be expected, increasing S-index is strongly correlated with the rate of detections.

4.2 $|B_\ell|$ Measurements

In Figure 3, we plot the maximum $|B_\ell|$ against T_{eff} for the sample of 19 newly-observed stars and the BCool planet-hosts superimposed on the entire BCool sample (data from Marsden et al. (2014)). Our results are consistent with the low activity area of the BCool sample.

In Figure 4, we similarly overplot our sample and BCool planet-hosts over the entire BCool survey for $|B_\ell|$ against $v \sin i$. As in Marsden et al. (2014, Fig. 13, Sec 6.3.3), stars above the dashed line are considered to have high values of $|B_\ell|$ compared to stars with a similar $v \sin i$. We note that only a single star in our new sample (HIP 28767) has a longitudinal magnetic field marginally above this line. It also has, by far, the highest S-index in our sample. Given the correlation of decreasing $|B_\ell|$ with increasing age it is not surprising that almost our entire sample is located below this cutoff line.

Table 6. Results from the analysis of the Stokes V LSD profiles of the stars not observed by Marsden et al. (2014). Column 3 provides the date of the observation (in the case of HIP 64457 two observations were obtained). Column 4 shows the radial velocity for the star (see 2); for comparison column 5 shows the radial velocity measured by Nidever et al. (2002) or in two cases from Valenti & Fischer (2005) indicated by $^{\text{VF}}$. Columns 6 and 7 show the signal-to-noise of the Stokes V profile and the number of lines used in the LSD process respectively. Column 8 indicates if the magnetic field was unambiguously detected (D) or not (N); note we have no marginal detections, represented by M in Marsden et al. (2014, Table 3). Column 9 shows the false alarm probability calculated for the detection in column 8. Columns 10 and 11 indicate the velocity range used to calculate B_{ℓ} (column 12) and N_{ℓ} (column 13) using equation 5.

HIP no.	Obs. no.	HJD +2450000	RV (this work) (km s $^{-1}$)	RV (Nidever) (km s $^{-1}$)	SNR $_{\text{LSD}}$	lines used	Detection	FAP	Velocity range (km s $^{-1}$)		B_{ℓ} (G)	N_{ℓ} (G)
14954	1	7033.33090	+19.64	+19.331	60048	11101	N	5.320×10^{-1}	+9	+31	$+0.4 \pm 0.3$	0.0 ± 0.3
17747	1	6958.50071	-9.97	-10.6 $^{\text{VF}}$	18483	10602	N	9.967×10^{-1}	-25	+5	$+1.2 \pm 1.1$	$+1.5 \pm 1.1$
24205	1	6926.67026	+5.74	+5.714	16164	7584	N	2.109×10^{-1}	+0	+13	$+1.3 \pm 0.4$	$+0.3 \pm 0.4$
25191	1	7034.43181	+29.54	-	6046	9392	N	4.518×10^{-1}	+18	+41	-2.3 ± 1.9	$+1.9 \pm 1.9$
26381	1	6957.55553	-22.93	-23.076	12834	9365	N	6.022×10^{-1}	-34	-13	-1.3 ± 1.2	$+2.3 \pm 1.2$
26664	1	6962.64066	-21.85	-	11787	12097	N	1.245×10^{-1}	-27	-16	-1.5 ± 0.5	$+0.3 \pm 0.5$
27253	1	6982.58476	+30.44	+30.210	28583	12803	D	2.509×10^{-9}	+23	+38	$+1.7 \pm 0.3$	$+0.0 \pm 0.3$
27384	1	6960.64135	-25.29	-	13887	13918	D	1.332×10^{-15}	-31	-20	$+3.4 \pm 0.4$	-0.1 ± 0.4
28767	1	6927.68776	+32.85	+32.542	20086	10062	D	1.448×10^{-9}	+14	+52	$+4.5 \pm 1.4$	$+3.5 \pm 1.4$
29301	1	6994.63288	-47.25	-	8003	8309	N	4.801×10^{-1}	-59	-36	-2.7 ± 1.7	$+1.0 \pm 1.7$
30057	1	6994.71807	-28.98	-	12649	9147	N	9.741×10^{-1}	-36	-22	$+0.5 \pm 0.6$	-0.5 ± 0.6
32916	1	6959.64396	+12.18	+12.045	14420	11084	N	3.266×10^{-2}	+5	+18	$+0.9 \pm 0.5$	-0.9 ± 0.5
45406	1	6995.69091	+20.08	-	14833	11058	N	9.316×10^{-1}	+9	+32	-1.5 ± 1.0	$+2.1 \pm 1.0$
64457	1	7030.70798	-11.80	-12.012	17873	13110	D	6.762×10^{-7}	-18	-5	$+2.5 \pm 0.4$	-0.5 ± 0.4
	2	7032.69851	-11.75	-12.012	21789	13048	D	5.749×10^{-13}	-18	-5	$+2.4 \pm 0.3$	-0.6 ± 0.3
95740	1	6995.28708	-50.16	-54.9 $^{\text{VF}}$	9290	10006	N	1.839×10^{-1}	-58	-41	$+3.0 \pm 0.9$	$+0.6 \pm 0.9$
96507	1	6982.30247	+0.82	-	14747	10618	N	5.742×10^{-1}	-7	+9	$+0.7 \pm 0.7$	$+0.9 \pm 0.7$
98767	1	6982.35222	-45.08	-45.308	25620	12051	N	9.512×10^{-1}	-50	-40	-0.2 ± 0.2	$+0.3 \pm 0.2$
101966	1	6984.27534	-30.80	-30.189	14961	9143	N	9.940×10^{-1}	-45	-16	$+1.7 \pm 1.23$	-0.3 ± 1.3
108859	1	6957.33207	-14.56	-14.759	11851	7164	N	4.666×10^{-1}	-23	-5	-0.9 ± 0.8	-0.6 ± 0.8

Table 7. Table of coefficients for Equation 6 as calculated by Marsden et al. (2014) for the NARVAL instrument.

Coefficient	NARVAL
a	12.873
b	2.502
c	8.877
d	4.271
e	1.183×10^{-3}

Figure 5 illustrates that once again, the planet hosting sample of this work is entirely consistent with the BCool survey results. In the upper panel of Figure 5, we show the magnetic field strength against the published ages of the stars (superimposed on the BCool sample) and in the lower panel, the magnetic field against the chromospheric age we derive. It is clear that our sample has older, evolved stars, and as expected their level of activity is lower than the younger stars which generate the more extreme magnetic fields.

Another general observation consistent with Marsden et al. (2014) is that cooler stars in our sample tend to have higher $|B_{\ell}|$. However it should be noted that there are only 5 K dwarfs in the combined set of planet-hosting stars.

Chromospheric activity seems to be the most strongly correlated with $|B_{\ell}|$, as shown in Figure 6. It should be noted that more active stars are generally excluded from planet-search programs, given that phenomena generated by stellar activity can mimic the cyclic variations used to detect planets (Saar & Donahue 1997; Saar et al. 1998; Jeffers et al. 2014), additionally biasing the entire sample to less ac-

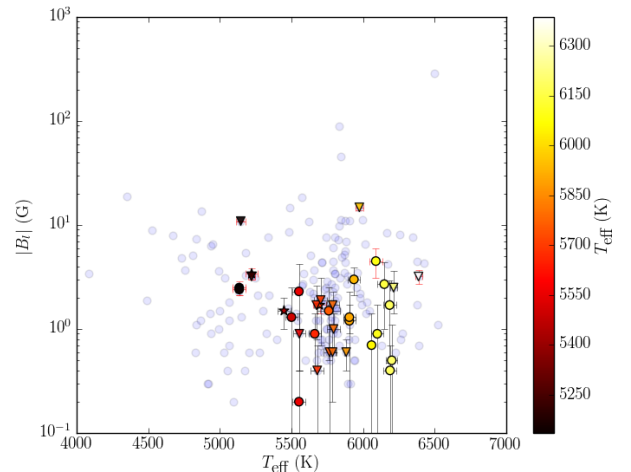


Figure 3. Plot of the maximum measured $|B_{\ell}|$ vs T_{eff} for the planet-hosting stars (symbols are as in Fig. 1). The complete BCool sample is shown as blue circles.

tive stars. Much work is currently underway in attempting to disentangle stellar activity signals from those generated from planetary sources (Petit et al. 2015; Feng et al. 2016; Hébrard et al. 2016; Herrero et al. 2016). This may in the future allow for a broadening of the sample set of planet-hosting stars.

Table 8. Chromospheric activity of the stars not observed by Marsden et al. (2014). $B - V$ and V values are from *Hipparcos*. Where Wright et al. (2004) has calculated an S-index, this is shown in column 3. Chromospheric ages, periods and $\log(P_{rot}/\tau)$ have been determined using the equations presented in Wright et al. (2004). As noted in the text, sample standard deviations are used as an indication in of various errors. Note that HIP 64457 (+) has two sequences of observations (8 exposures) compared with all other targets (4 exposures).

HIP no.	$B - V$ (Hipparcos)	V	S-index Wright.	S-index (this work)	$\log(R'_{HK})$	Chromospheric Age (Gyr)	Chromospheric period (d)	Ca _{IRT} -index	H _{α} -index	$\log(P_{rot}/\tau)$
14954	0.575	5.07	0.173	0.1569 ± 0.0003	$-4.99^{+0.00}_{-0.00}$	$5.404^{+0.051}_{-0.044}$	$16.1^{+0.0}_{-0.0}$	0.7411 ± 0.0011	0.3057 ± 0.0001	$+0.320^{+0.001}_{-0.001}$
17747	0.634	7.25	0.150	0.1451 ± 0.0004	$-5.10^{+0.00}_{-0.01}$	$7.814^{+0.132}_{-0.079}$	$25.4^{+0.1}_{-0.1}$	0.7561 ± 0.0008	0.3106 ± 0.0001	$+0.361^{+0.002}_{-0.001}$
24205	0.588	7.00	0.180	0.1773 ± 0.0011	$-4.87^{+0.01}_{-0.00}$	$3.515^{+0.049}_{-0.105}$	$15.5^{+0.1}_{-0.2}$	0.8209 ± 0.0009	0.3146 ± 0.0002	$+0.266^{+0.002}_{-0.004}$
25191	0.761	8.99	—	0.1558 ± 0.0085	$-5.05^{+0.05}_{-0.07}$	$6.777^{+1.622}_{-1.069}$	$39.4^{+2.4}_{-1.6}$	0.8139 ± 0.0031	0.3307 ± 0.0019	$+0.344^{+0.026}_{-0.018}$
26381	0.667	7.68	0.179	0.1881 ± 0.0016	$-4.86^{+0.01}_{-0.01}$	$3.314^{+0.078}_{-0.078}$	$23.5^{+0.2}_{-0.2}$	0.8462 ± 0.0007	0.3292 ± 0.0006	$+0.257^{+0.004}_{-0.004}$
26664	0.827	8.67	—	0.1866 ± 0.0049	$-4.94^{+0.02}_{-0.02}$	$4.524^{+0.397}_{-0.253}$	$40.3^{+1.0}_{-0.6}$	0.7546 ± 0.0004	0.3401 ± 0.0008	$+0.299^{+0.010}_{-0.007}$
27253	0.773	5.95	0.174	0.1750 ± 0.0005	$-4.96^{+0.00}_{-0.00}$	$4.854^{+0.056}_{-0.036}$	$37.3^{+0.1}_{-0.1}$	0.6871 ± 0.0007	0.3231 ± 0.0001	$+0.308^{+0.001}_{-0.001}$
27384	0.873	8.26	—	0.1978 ± 0.0046	$-4.93^{+0.01}_{-0.02}$	$4.393^{+0.290}_{-0.240}$	$42.3^{+0.8}_{-0.7}$	0.7187 ± 0.0006	0.3368 ± 0.0005	$+0.296^{+0.008}_{-0.007}$
28767	0.573	6.74	0.234	0.2543 ± 0.0003	$-4.58^{+0.00}_{-0.00}$	$1.249^{+0.002}_{-0.005}$	$7.8^{+0.0}_{-0.0}$	0.8398 ± 0.0017	0.3138 ± 0.0002	$+0.011^{+0.001}_{-0.002}$
29301	0.530	8.68	—	0.1384 ± 0.0028	$-5.13^{+0.04}_{-0.01}$	$8.752^{+0.392}_{-1.088}$	$12.9^{+0.2}_{-0.5}$	0.7734 ± 0.0010	0.3041 ± 0.0008	$+0.375^{+0.006}_{-0.016}$
30057	0.596	8.03	—	0.1492 ± 0.0019	$-5.05^{+0.01}_{-0.02}$	$6.763^{+0.466}_{-0.290}$	$19.6^{+0.3}_{-0.2}$	0.7451 ± 0.0006	0.3076 ± 0.0002	$+0.345^{+0.008}_{-0.005}$
32916	0.729	8.10	0.211	0.1858 ± 0.0012	$-4.90^{+0.01}_{-0.01}$	$3.824^{+0.090}_{-0.076}$	$31.0^{+0.2}_{-0.2}$	0.7615 ± 0.0009	0.3281 ± 0.0003	$+0.278^{+0.003}_{-0.003}$
45406	0.693	8.05	—	0.1493 ± 0.0013	$-5.08^{+0.01}_{-0.01}$	$7.346^{+0.286}_{-0.262}$	$32.6^{+0.3}_{-0.3}$	0.7730 ± 0.0009	0.3222 ± 0.0003	$+0.354^{+0.005}_{-0.004}$
64457 ⁺	0.930	7.56	0.215	0.2033 ± 0.0032	$-4.96^{+0.01}_{-0.01}$	$4.896^{+0.207}_{-0.184}$	$45.4^{+0.5}_{-0.5}$	0.7618 ± 0.0018	0.3528 ± 0.0007	$+0.309^{+0.005}_{-0.004}$
95740	0.678	7.86	0.145	0.1521 ± 0.0027	$-5.06^{+0.02}_{-0.02}$	$6.811^{+0.450}_{-0.509}$	$30.1^{+0.5}_{-0.6}$	0.7634 ± 0.0007	0.3171 ± 0.0005	$+0.346^{+0.007}_{-0.008}$
96507	0.606	6.67	—	0.1286 ± 0.0009	$-5.26^{+0.01}_{-0.02}$	$12.638^{+0.559}_{-0.214}$	$25.4^{+0.5}_{-0.2}$	0.7486 ± 0.0021	0.3110 ± 0.0001	$+0.430^{+0.008}_{-0.003}$
98767	0.749	5.73	0.148	0.1499 ± 0.0018	$-5.08^{+0.01}_{-0.01}$	$7.461^{+0.354}_{-0.321}$	$39.2^{+0.5}_{-0.4}$	0.7657 ± 0.0019	0.3324 ± 0.0003	$+0.356^{+0.005}_{-0.005}$
101966	0.559	6.39	0.151	0.1455 ± 0.0014	$-5.07^{+0.01}_{-0.01}$	$7.213^{+0.332}_{-0.334}$	$15.5^{+0.2}_{-0.2}$	0.7701 ± 0.0010	0.3039 ± 0.0006	$+0.352^{+0.005}_{-0.005}$
108859	0.594	7.65	0.154	0.1558 ± 0.0085	$-5.01^{+0.06}_{-0.09}$	$5.831^{+1.886}_{-1.193}$	$18.6^{+1.5}_{-1.0}$	0.8025 ± 0.0023	0.3112 ± 0.0003	$+0.326^{+0.033}_{-0.024}$

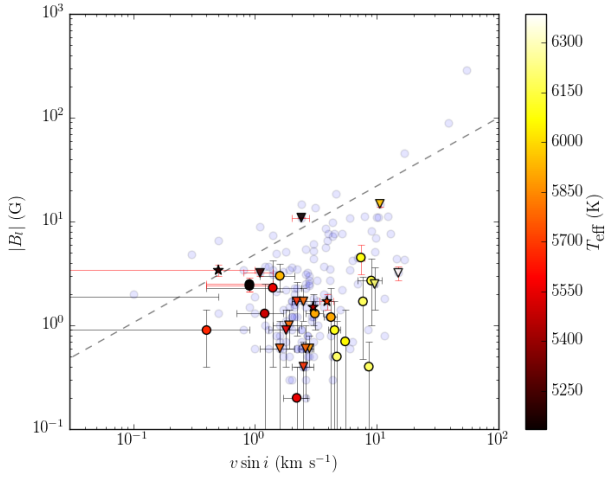


Figure 4. Plot of the maximum measured $|B_{\ell}|$ vs $v \sin i$ for the planet-hosting stars (symbols are as in Fig. 1). Stars located above the dashed line have significantly higher $|B_{\ell}|$ than others with similar $v \sin i$, as per Marsden et al. (2014, Sec. 6.3.3). The complete BCool sample is shown as blue circles.

4.3 Planetary Influences

In Figure 7, we present the configuration of the planetary systems from both our new sample and the BCool sample, and their relationship with the activity proxy (S-index) and the magnetic field [$\log(|B_{\ell}|)$]. In both panels, each circle represents a planet, and its centre point on the x-axis represents the semi-major axis of its orbit. In the case of systems with

more than one planet, each planet is represented, with all planets in a system having the same y-axis value. The size of the circles is proportional to the planetary mass. In the upper panel, the y-axis represents the magnetic field strength of the host star and the colour of the circle its S-index. In the lower panel, the y-axis represents the S-index of the host star and the colour of the circle is $\log(|B_{\ell}|)$. Finally if a magnetic detection occurred for a host star, the circle(s) representing its planet(s) are outlined in red. There appears to be no correlation between the magnetic field strength and the planetary configuration.

There are several planets which would warrant the colloquial appellation of “hot Jupiter”, and would therefore seem the most likely candidates for star-planet interaction, whether through tidal effects, magnetic interaction, or other posited SPI mechanisms. However, the presence of these planets do not result in any detectable trend towards higher activity or higher measured longitudinal magnetic field. This is consistent with the findings of Miller et al. (2015).

Indeed investigating potential tidal effects in particular, if we plot $\log(|B_{\ell}|)$ versus the logarithm of the mass ratio (planetary mass divided by the orbital semi-major axis), shown in Figure 8, there appears to be a weak positive linear relationship. This should be interpreted with some caution, given the very low R^2 value and the 95% confidence interval. This confidence interval provides an estimate of the uncertainty around the proposed relationship, and indicates that the population relationship may be zero. Plotting $\log(|B_{\ell}|)$ against the logarithm of the relative height of the tidal bulge induced on the star (h_t from Figueira et al. (2016, Eq. 1)) shows absolutely no correlation (Fig. 9).

It is noted that the sample is small, and while there are some “hot Jupiters” none of them are at the higher end of the

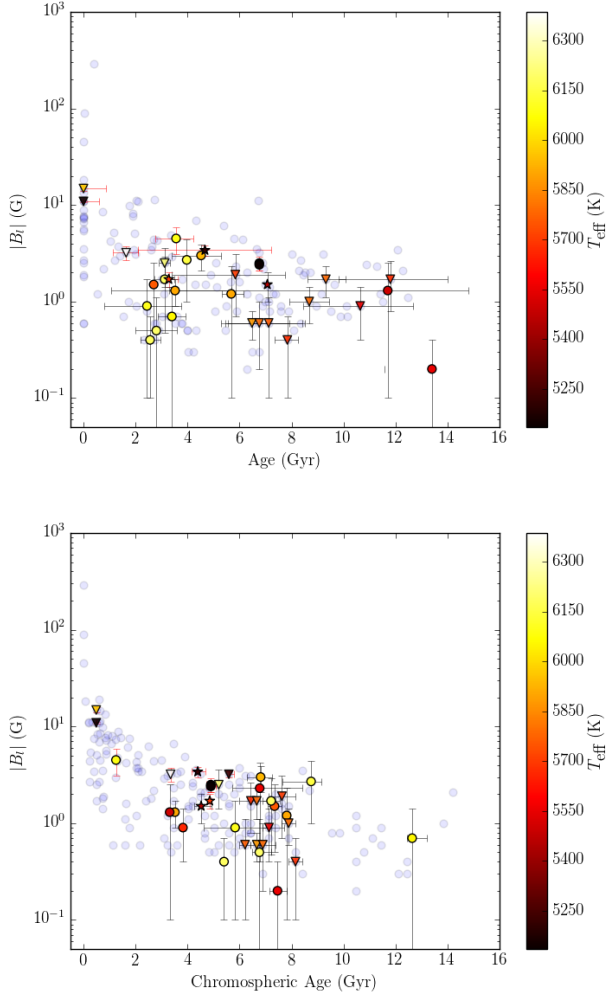


Figure 5. Plot of maximum measured $|B_\ell|$ vs Age (upper panel) and Chromospheric Age (lower panel; calculated from the equations of [Wright et al. \(2004\)](#) and shown in [Table 8](#)) for the planet-hosting stars. Symbols are as in [Fig. 1](#). The complete BCoolest sample is shown as blue circles.

mass range, nor are the more massive planets particularly close to the host star. Given the correlations between stellar parameters and the strength of the stellar magnetic field detailed by [Marsden et al. \(2014\)](#), it is clear that any effect of SPI on the global stellar magnetic field or activity proxies measured here, if it exists, is too subtle to detect in our sample. [Fares et al. \(2013\)](#) and [Vidotto et al. \(2014\)](#) came to similar conclusions and called for larger samples. However, the inherent biases in planet-search programs which exclude active stars makes increasing the sample size and scope difficult. Alternatively, in the absence of a larger sample, increasing the amount of observations of both the set of planet-hosting and non-planet-hosting stars would allow us to analyse the full magnetic variability range for each star and to look for influence on any magnetic cycles.

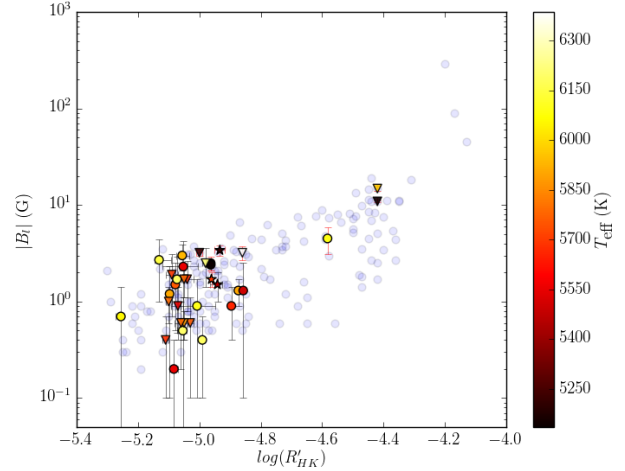


Figure 6. Plot of maximum measured $|B_\ell|$ vs $\log(R'_{HK})$ ([Table 8](#)) for the planet-hosting stars. Symbols are as in [Fig. 1](#). The complete BCoolest sample is shown as blue circles.

5 CONCLUSIONS

We have presented an investigation of the large-scale magnetic field of 19 additional solar-type stars for the BCoolest survey ([Marsden et al. 2014](#)). We expanded our sample of planet-hosting stars by adding the previously-observed planet host in the BCoolest survey. The results we obtain for these stars are congruent with the wider BCoolest survey. The selection by planet-search surveys of low activity, mature stars biases the sample of stars with discovered planets towards those with higher ages and lower intrinsic activity. Consequently, we obtain a lower rate of magnetic detections, and of lower measures of $|B_\ell|$, the longitudinal magnetic field, than the wider survey of 170 solar-type stars.

While we cannot rule out that the presence of the planets around these host stars has an effect on the host star's magnetic field, we show that such an effect is too subtle to detect in our sample. A larger sample of planet-hosting solar-type stars may reveal a trend. If a trend exists, there may be a lower limit to the planetary mass and upper limit to the semi-major axis of the planetary orbit for which any SPI becomes apparent using these methods. Further target selection should perhaps focus on massive hot Jupiter systems to further investigate these limits.

The four planetary systems for which we have made magnetic detections may be candidates for long-term magnetic topology monitoring (see [Appendix A](#)). Observation of the magnetic field of the host star may allow for modelling of the space weather environment of its planetary system ([Vidotto et al. 2015](#); [Nicholson et al. 2016](#); [Alvarado-Gómez et al. 2016](#)). Also, with these known magnetic fields, it may be possible to determine whether other methods, such as radio observations, may be able to detect magnetic interactions between star and planet, or to at least place limits on the expected signals one may expect from such behaviour ([Fares et al. 2010](#); [Vidotto et al. 2012](#); [See et al. 2015](#); [Vidotto et al. 2015](#)).

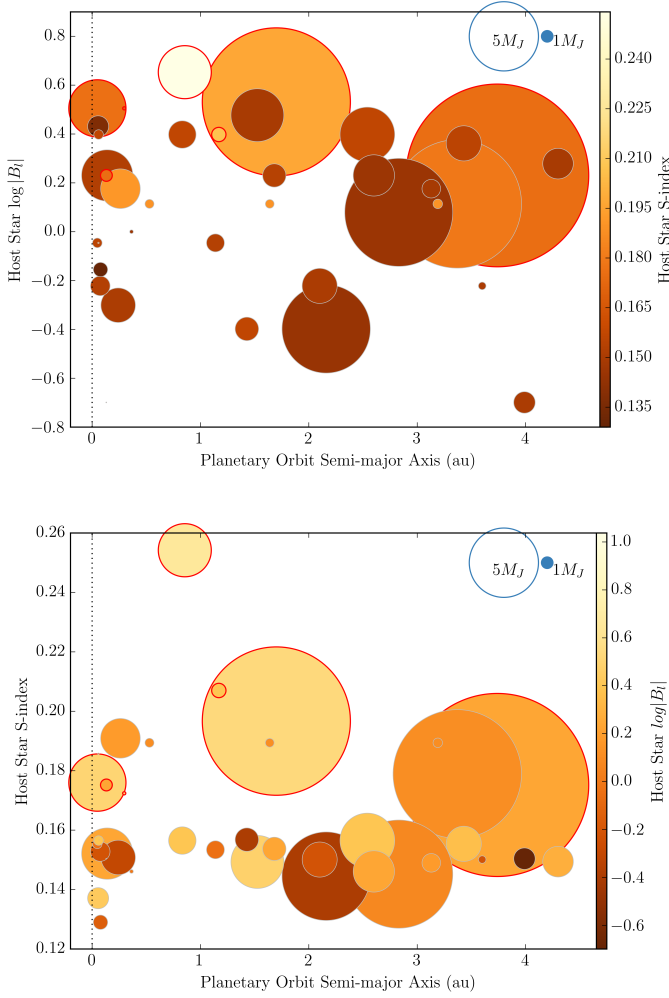


Figure 7. S-index and $\log(|B_\ell|)$ shown against the semi-major axis of planetary orbits for the BCool planet hosting stars and the new survey targets. The fill colours of the circles represent $\log(|B_\ell|)$ (upper panel) and S-index (lower panel). The radius of circles are proportional to planetary masses, $M \sin i$. Red edges to the circle indicates the host star had a magnetic detection. HIP107350 (HN Peg) and HIP16537 (ϵ Eri) are not included on this plot for clarity. HN Peg b has a semi-major axis of ~ 790 au, and ϵ Eri has a relatively high S-index (0.5357) compared to the other sample stars; both have magnetic detections and $\log(|B_\ell|)$ much higher than all other stars shown. We find no detectable correlation between mass and orbital distance of the planets in the system and the activity of the star.

ACKNOWLEDGMENTS

This work was based on observations obtained with NARVAL at the T el escope Bernard Lyot (TBL). TBL/NARVAL are operated by INSU/CNRS.

SVJ acknowledges research funding by the Deutsche Forschungsgemeinschaft (DFG) under grant SFB 963/1, project A16.

The Strategic Research Funding for the Starwinds project provided by the University of Southern Queensland provides resources to the Astrophysics group within the Computational Engineering and Science Research Cen-

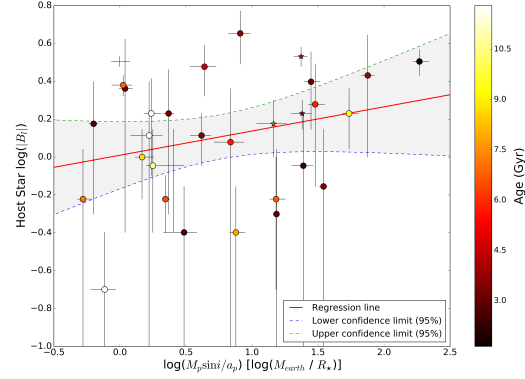


Figure 8. $\log(|B_\ell|)$ shown against mass ratio for the BCool planet hosting stars and the new survey targets. Points are coloured according to age. Note there is a very weak positive linear relationship (see regression line). The shaded area represents the 95% confidence interval. Within this confidence interval, the population relationship may be zero. The young, active stars HIP107350 (HN Peg) and HIP16537 (ϵ Eri) are not included on this plot for clarity.

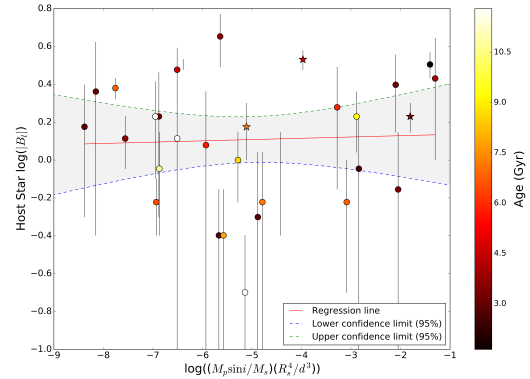


Figure 9. $\log(|B_\ell|)$ shown against the log of the relative tidal height (h_t) for the BCool planet hosting stars and the new survey targets. Points are coloured according to age. Horizontal error bars have been omitted for clarity. No trend is apparent, although a regression line is shown. The shaded area represents the 95% confidence interval around the regression line. The young, active stars HIP107350 (HN Peg) and HIP16537 (ϵ Eri) are not included on this plot for clarity.

tre at USQ (MWM, SCM, BDC). MWM is supported by an Australian Postgraduate Award Scholarship.

This research has made use of NASA’s Astrophysics Data System. This research has made use of the SIMBAD database, operated at CDS, Strasbourg, France. This research has made use of the VizieR catalogue access tool, CDS, Strasbourg, France. This work has made use of the VALD database, operated at Uppsala University, the Institute of Astronomy RAS in Moscow, and the University of Vienna.

The authors would like to thank Victor See and Colin Folsom for their helpful comments and suggestions on the

original manuscript. Further thanks to the BCool collaboration.

REFERENCES

- Alvarado-Gómez J. D., Hussain G. A. J., Cohen O., Drake J. J., Garraffo C., Grunhut J., Gombosi T. I., 2016, *A&A*, 594, A95
- Aurière M., 2003, in Arnaud J., Meunier N., eds, *EAS Pub. Ser. Vol. 9, Magnetism and Activity of the Sun and Stars*. p. 105
- Bagnulo S., Landolfi M., Landstreet J. D., Landi Degl’Innocenti E., Fossati L., Sterzik M., 2009, *PASP*, 121, 993
- Beatty T. G., et al., 2012, *ApJ*, 756, L39
- Benedict G. F., et al., 2006, *ApJ*, 132, 2206
- Butler R. P., et al., 2006, *ApJ*, 646, 505
- Casagrande L., Schönrich R., Asplund M., Cassisi S., Ramírez I., Meléndez J., Bensby T., Feltzing S., 2011, *A&A*, 530, A138
- Chauvin G., Beust H., Lagrange A.-M., Eggenberger A., 2011, *A&A*, 528, A8
- Cuntz M., Saar S. H., Musielak Z. E., 2000, *ApJ*, 533, L151
- Díaz R. F., et al., 2016, *A&A*, 585, A134
- Donati J.-F., Semel M., Rees D. E., 1992, *A&A*, 265, 669
- Donati J.-F., Semel M., Carter B. D., Rees D. E., Cameron A. C., 1997, *MNRAS*, 291, 658
- Fares R., et al., 2010, *MNRAS*, 406, 409
- Fares R., Moutou C., Donati J.-F., Catala C., Shkolnik E. L., Jardine M. M., Cameron A. C., Deleuil M., 2013, *MNRAS*, 435, 1451
- Feng F., Tuomi M., Jones H. R. A., Butler R. P., Vogt S., 2016, *Monthly Notices of the Royal Astronomical Society*, 461, 2440
- Figueira P., et al., 2016, *A&A*, 592, A143
- France K., et al., 2016, *ApJ*, 820, 89
- Gizis J. E., Reid I. N., Hawley S. L., 2002, *ApJ*, 123, 3356
- Gregory P. C., Fischer D. A., 2010, *MNRAS*, 403, 731
- Harakawa H., et al., 2010, *ApJ*, 715, 550
- Hébrard É. M., Donati J.-F., Delfosse X., Morin J., Moutou C., Boisse I., 2016, *Monthly Notices of the Royal Astronomical Society*, 461, 1465
- Herrero E., Ribas I., Jordi C., Morales J. C., Perger M., Rosich A., 2016, *A&A*, 131, 1
- Horner J., Jones B., 2010, *International Journal of Astrobiology*, 9, 273
- Isaacson H., Fischer D., 2010, *ApJ*, 725, 875
- Jeffers S. V., Barnes J. R., Jones H. R. A., Reiners A., Pinfield D. J., Marsden S. C., 2014, *MNRAS*, 438, 2717
- Jofré E., Petrucci R., Saffe C., Saker L., Artur de la Villarmois E., Chavero C., Gómez M., Mauas P. J. D., 2015, *A&A*, 574, A50
- Kochukhov O., Makaganiuk V., Piskunov N. E., 2010, *A&A*, 524, A5
- Krejčová T., Budaj J., 2012, *A&A*, 540, A82
- Kupka F. G., Ryabchikova T. A., Piskunov N. E., Stempels H. C., Weiss W. W., 2000, *Baltic Astronomy*, 9, 590
- Lanza A. F., 2009, *A&A*, 505, 339
- Lanza A. F., 2012, *A&A*, 544, 23
- Lanza A. F., et al., 2011, *A&A*, 525, A14
- Luhman K. L., et al., 2007, *ApJ*, 654, 570
- Marsden S. C., et al., 2014, *MNRAS*, 444, 3517
- Martíoli E., McArthur B. E., Benedict G. F., Bean J. L., Harrison T. E., Armstrong a., 2010, *ApJ*, 708, 625
- Mathys G., 1989, *Fundamentals Cosmic Phys.*, 13, 143
- McDonald I., Zijlstra A. A., Boyer M. L., 2012, *MNRAS*, 427, 343
- Miller B. P., Gallo E., Wright J. T., Pearson E. G., 2015, *ApJ*, 799, 163
- Morin J., et al., 2008, *MNRAS*, 390, 567
- Moutou C., et al., 2006, *A&A*, 458, 327
- Moutou C., et al., 2007, *A&A*, 473, 651
- Naef D., et al., 2010, *A&A*, 523, A15
- Nicholson B. A., et al., 2016, *MNRAS*, 459, 1907
- Nidever D. L., Marcy G. W., Butler R. P., Fischer D. A., Vogt S. S., 2002, *ApJS*, 141, 503
- Petit P., Donati J.-F., the ESPaDOnS Project Team 2003, in Arnaud J., Meunier N., eds, *EAS Pub. Ser. Vol. 9, Magnetism and Activity of the Sun and Stars*. p. 97
- Petit P., Aurière M., Konstantinova-Antova R., Morgenthaler A., Perrin G., Roudier T., Donati J.-F., 2013, in Rozelot J.-P., Neiner C., eds, *Lecture Notes in Physics*, Berlin Springer Verlag Vol. 857, *Lecture Notes in Physics*, Berlin Springer Verlag. p. 231 ([arXiv:1109.3979](https://arxiv.org/abs/1109.3979))
- Petit P., et al., 2015, *A&A*, 584, A84
- Pillitteri I., Wolk S. J., Cohen O., Kashyap V., Knutson H., Lisse C. M., Henry G. W., 2010, *ApJ*, 722, 1216
- Quillen A. C., Thorndike S., 2002, *ApJ*, 578, L149
- Robertson P., et al., 2012, *ApJ*, 749, 39
- Rubenstein E. P., Schaefer B. E., 2000, *ApJ*, 529, 1031
- Saar S. H., Donahue R. A., 1997, *The Astrophysical Journal*, 485, 319
- Saar S. H., Butler R. P., Marcy G. W., 1998, *The Astrophysical Journal*, 498, L153
- Schneider J., Dedieu C., Le Sidaner P., Savalle R., Zolotukhin I., 2011, *A&A*, 532, 79
- See V., Jardine M., Fares R., Donati J.-F., Moutou C., 2015, *MNRAS*, 450, 4323
- Shkolnik E. L., 2013, *ApJ*, 766, 9
- Shkolnik E., Walker G. A. H., Bohlender D. A., Gu P. G., Kürster M., 2005, *ApJ*, 622, 1075
- Shkolnik E., Bohlender D. A., Walker G. A. H., Collier Cameron A., 2008, *ApJ*, 676, 628
- Shorlin S. L. S., Wade G. A., Donati J.-F., Landstreet J. D., Petit P., Sigut T. A. A., Strasser S., 2002, *A&A*, 392, 637
- da Silva R., et al., 2007, *A&A*, 473, 323
- Strugarek A., Brun A. S., Matt S. P., Réville V., 2015, *ApJ*, 815, 111
- Takeda G., Ford E. B., Sills A., Rasio F. A., Fischer D. A., Valenti J. A., 2007, *ApJS*, 168, 297
- Valenti J. A., Fischer D. A., 2005, *ApJS*, 159, 141
- Vidotto A. A., Fares R., Jardine M., Donati J.-F., Opher M., Moutou C., Catala C., Gombosi T. I., 2012, *MNRAS*, 423, 3285
- Vidotto A. A., et al., 2014, *MNRAS*, 441, 2361
- Vidotto A. A., Fares R., Jardine M., Moutou C., Donati J. F., 2015, *MNRAS*, 449, 4117
- Wang S. X., et al., 2012, *ApJ*, 761, 46
- Wenger M., et al., 2000, *A&AS*, 143, 9
- Wright J. T., Marcy G. W., Butler R. P., Vogt S. S., 2004, *ApJS*, 152, 261
- Wright J. T., et al., 2007, *ApJ*, 657, 533

APPENDIX A: MAGNETIC DETECTIONS

A1 HIP 27253 (HD 38529)

The star HIP 27253 (G8III/IV; $T_{eff} = 5697 \pm 44$ K) is known to host two planets. HD 38529b has a minimum mass $\sim 0.85 M_J$, and orbits at a distance of ~ 0.13 au, while the much more massive HD 38529c ($\sim 13 M_J$) orbits at approximately 3.75 au. HIP 27253 has the lowest S-index of the four stars for which we obtained detections (0.1750 ± 0.0005). It is relatively bright ($V \sim 6$) compared with the remainder of the sample, with over 12000 lines used in the LSD process, resulting in a relatively high SNR_{LSD} of ~ 28000 .

One of the two subgiants for which we obtained a magnetic detection, Takeda et al. (2007) place its age at over 3 Gyr, whilst we derive a chromospheric age of ~ 4.8 Gyr.

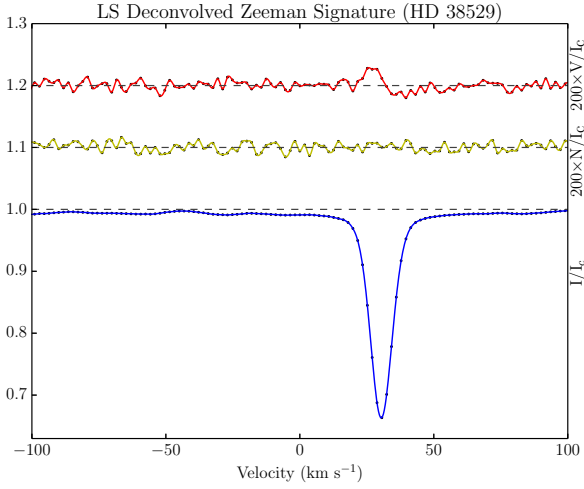


Figure A1. Plot of the LSD profiles of HIP 27253 (HD 38529). The upper line (in red) is the Stokes V profile, expanded 200 times and shifted up by 0.2. The centre line (yellow) represents the LSD null profile also expanded by 200 and shifted up 0.1. The lower line (in blue) shows the Stokes I (intensity) LSD profile.

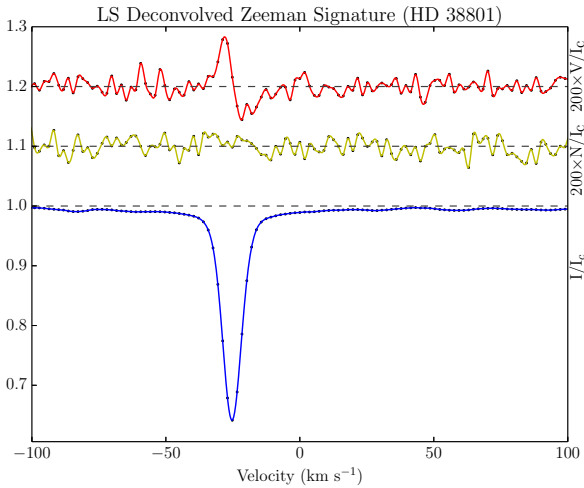


Figure A2. Plot of LSD profiles for HIP 27384 (HD 38801). The plot is described in Figure A1.

An older subgiant star with a close Jupiter mass planet, HIP 27253 would be an interesting target for further investigation. The LSD profile including Stokes V , Stokes I and null (N) profiles is shown in Figure A1.

A2 HIP 27384 (HD 38801)

HIP 27384 (G8IV; $T_{eff} = 5222 \pm 44$ K) is the second of our two subgiants which have a magnetic detection (LSD profiles shown in Fig. A2). A single large planet HD 38801b with a mass of $\sim 10.7 M_J$ orbits the star at 1.7 au. A mature star with age measurements > 4 Gyr, HIP 27384 has one of the largest $|B_\ell|$ measurements in our sample. Its low $v \sin i \approx 0.5 \text{ km s}^{-1}$ makes tomographic mapping of the surface magnetic field challenging.

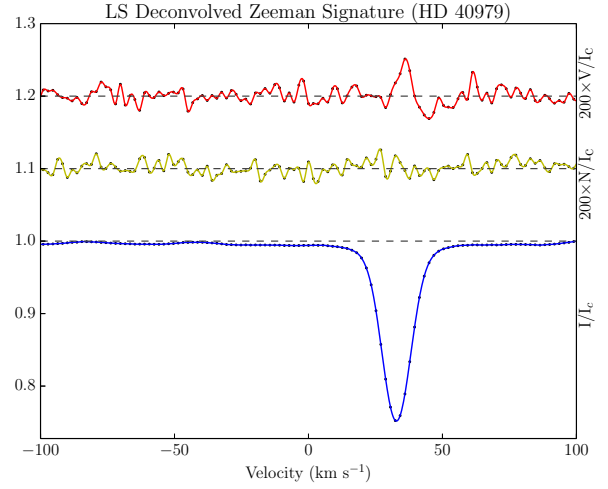


Figure A3. Plot of LSD profiles for HIP 28767 (HD 40979). The plot is described in Figure A1.

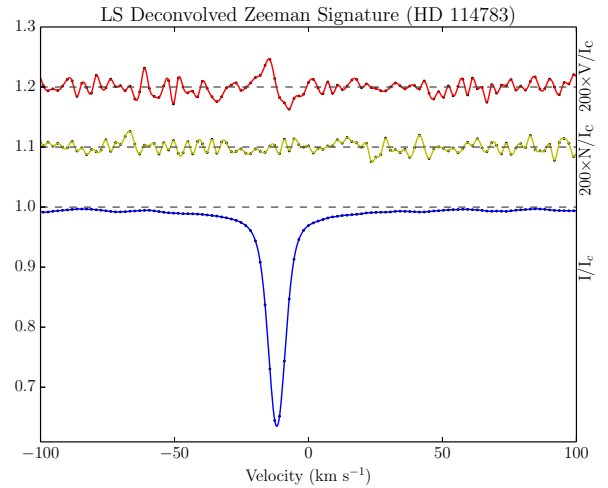


Figure A4. Plot of LSD profiles for HIP 64457 (HD 114783). The plot is described in Figure A1.

A3 HIP 28767 (HD 40979)

HIP 28767 (F8; $T_{eff} = 6089 \pm 44$ K) has by far the highest S-index of the sample (0.2543 ± 0.0003), and consequently it is not surprising that a magnetic field was detected. A significant field in the null profile ($|N_\ell|$) relative to the size of the measured $|B_\ell|$ means that followup observations may be necessary to confirm the actual level of the longitudinal field with more confidence. The hottest star in our sample to have a detection, HIP 28767 has a $\sim 3.8 M_J$ planet (HD 40979b) orbiting at a distance of ~ 0.85 au. The Stokes V , Stokes I and N profiles for HIP 28767 are shown in Figure A3.

A4 HIP 64457 (HD 114783)

Two observations of HIP 64457 (K1V; $T_{eff} = 5135 \pm 44$ K) were taken during the observing period, and the set of LSD profiles from the second observation (taken at \approx HJD 2457032.7) is shown in Figure A4. HD 114783b, with a mass approximately that of Jupiter orbits the star

at a distance of ~ 1.1 au. As one of the two stars (the other being HIP 28767; Sec. A3) with an S-index above 0.2, it was likely to provide a magnetic detection. With a similar temperature and rotation rate, a comparison of the magnetic activity and/or cycles of HIP 64457 and HIP 27384 (Sec. A2) may provide an insight into any apparent differences or similarities of dynamo between dwarfs and subgiants.

APPENDIX B: PLANET HOSTS FROM BCOOL SURVEY

Table B1. Planetary parameters of the sample of planet-hosting solar type stars from the BCool survey (Marsden et al. 2014), as an extension of Table 1. The stellar component’s *Hipparcos* number, SPOCS catalogue number and HD number (where applicable) are shown in the first three columns. Column 4 refers to the Name by which the planetary components (column 5) are known. The period, mass ($M \sin i$) and semi-major axis is shown for each planet. These values are from the references listed in the last column.

Star			Planet(s)						Refs.
HIP no.	SPOCS no.	HD no.	Name	Component	Period (d)	$M \sin i$ (M_J)	Semi-major axis (au)		
1499	13	1461	HD 1461	b	5.77152 ± 0.00045	0.0203 ± 0.0019	0.0634 ± 0.0022	2	
			HD 1461	c	13.5052 ± 0.0029	0.0176 ± 0.0023	0.1117 ± 0.0039	2	
3093	26	3651	54 Psc	b	62.206 ± 0.021	0.227 ± 0.023	0.296 ± 0.017	1	
7513	85	9826	<i>v</i> And	b	4.617113 ± 0.000082	0.687 ± 0.058	0.0595 ± 0.0034	1	
			<i>v</i> And	c	241.23 ± 0.30	1.98 ± 0.17	0.832 ± 0.048	1	
			<i>v</i> And	d	1290.1 ± 8.4	3.95 ± 0.33	2.54 ± 0.15	1	
8159	97	10697	HD 10697	b	1076.4 ± 2.4	6.38 ± 0.53	2.16 ± 0.12	1	
12048	128	16141	HD 16141	b	75.523 ± 0.055	0.260 ± 0.028	0.363 ± 0.021	1	
16537 ⁺	171	22049	ϵ Eri	b	2502 ± 10	0.78 ± 0.08	3.39 ± 0.36	3	
53721	472	95128	47 Uma	b	1078^{+2}_{-2}	$2.53^{+0.07}_{-0.06}$	$2.100^{+0.02}_{-0.02}$	4	
			47 Uma	c	2391^{+100}_{-87}	$0.540^{+0.066}_{-0.073}$	$3.6^{+0.1}_{-0.1}$	4	
			47 Uma	d	14002^{+4018}_{-5095}	$1.64^{+0.29}_{-0.48}$	$11.6^{+2.1}_{-2.9}$	4	
67275	577	120136	τ Boö	b	3.312463 ± 0.000014	4.13 ± 0.34	0.0481 ± 0.0028	1	
96901	855	186427	16 Cyg B	b	798.5 ± 1.0	1.68 ± 0.15	1.681 ± 0.097	1	
100970	894	195019	HD 195019	b	18.20163 ± 0.00040	3.70 ± 0.30	0.1388 ± 0.0080	5	
107350*	942	206860	HN Peg	b		16.0 ± 9.4	795.0 ± 15.0	6	
109378	960	210277	HD 210277	b	442.19 ± 0.50	1.29 ± 0.11	1.138 ± 0.066	1	
113357	990	217014	51 Peg	b	4.230785 ± 0.000036	0.472 ± 0.039	0.0527 ± 0.0030	1	
113421	992	217107	HD 217107	b	7.12690 ± 0.00022	1.41 ± 0.12	0.0748 ± 0.0043	1	
			HD 217107	c	3200 ± 1000	2.21 ± 0.66	4.3 ± 1.2	1	

References: 1: Butler et al. (2006), 2: Díaz et al. (2016), 3: Benedict et al. (2006), 4: Gregory & Fischer (2010), 5: Wright et al. (2007), 6: Luhman et al. (2007).

⁺ - HIP16537 (ϵ Eri) is suspected to host a second planet (Quillen & Thorndike 2002).

* - The planet orbiting HIP107530 (HN Peg) was discovered by direct imaging, and as a result, its orbital parameters unclear; semi-major axis is therefore taken as the projected separation (Luhman et al. 2007).

Table B2. Stellar parameters of the sample of planet-hosting solar type stars from the BCool survey (Marsden et al. 2014, Table 1), as an extension of Table 2. The spectral type is from SIMBAD (<http://simbad.u-strasbg.fr/simbad/>, Wenger et al. (2000)). Column 11 is the radius of the convective zone of the star. Values are found in the references shown in the final column of the table; locations where values were unavailable in the literature, are denoted by ‘X’.

HIP no.	SPOCS no.	Spec. Type	T_{eff} (K)	$\log(g)$ (cm s^{-2})	[M/H]	$\log(\text{Lum})$ (L_{\odot})	Age (Gyr)	Mass (M_{\odot})	Radius (R_{\odot})	Radius _{CZ} (R_{\odot})	$v \sin i$ (km s^{-1})	Refs.
1499	13	G0V	5765^{+44}_{-44}	$4.37^{+0.03}_{-0.03}$	$+0.16^{+0.03}_{-0.03}$	$+0.078^{+0.041}_{-0.041}$	$7.12^{+1.40}_{-1.56}$	$1.026^{+0.040}_{-0.030}$	$1.11^{+0.04}_{-0.04}$	$0.323^{+0.019}_{-0.020}$	$1.6^{+0.5}_{-0.5}$	1,2
3093	26	K0V	5221^{+25}_{-25}	$4.51^{+0.02}_{-0.01}$	$+0.16^{+0.02}_{-0.02}$	$-0.286^{+0.018}_{-0.018}$	X	$0.882^{+0.026}_{-0.021}$	$0.88^{+0.03}_{-0.02}$	$0.296^{+0.006}_{-0.009}$	$1.1^{+0.3}_{-0.3}$	1,2
7513	85	F9V	6213^{+22}_{-22}	$4.16^{+0.02}_{-0.04}$	$+0.12^{+0.01}_{-0.01}$	$+0.522^{+0.021}_{-0.021}$	$3.12^{+0.20}_{-0.24}$	$1.310^{+0.021}_{-0.014}$	$1.64^{+0.04}_{-0.05}$	$0.315^{+0.028}_{-0.073}$	$9.6^{+0.3}_{-0.3}$	1,2
8159	97	G5IV	5680^{+44}_{-44}	$4.03^{+0.03}_{-0.03}$	$+0.10^{+0.03}_{-0.03}$	$+0.448^{+0.054}_{-0.054}$	$7.84^{+0.40}_{-0.48}$	$1.112^{+0.026}_{-0.020}$	$1.73^{+0.06}_{-0.07}$	$0.568^{+0.038}_{-0.032}$	$2.5^{+0.5}_{-0.5}$	1,2
12048	128	G5IV	5794^{+44}_{-44}	$4.19^{+0.04}_{-0.04}$	$+0.09^{+0.03}_{-0.03}$	$+0.30^{+0.10}_{-0.10}$	$8.68^{+0.76}_{-0.76}$	$1.052^{+0.026}_{-0.022}$	$1.39^{+0.07}_{-0.07}$	$0.416^{+0.030}_{-0.028}$	$1.9^{+0.5}_{-0.5}$	1,2
16537	171	K2Vk:	5146^{+31}_{-31}	$4.61^{+X}_{-0.02}$	$+0.00^{+0.02}_{-0.02}$	$-0.486^{+0.011}_{-0.011}$	$0.00^{+0.60}_{-0.00}$	$0.856^{+0.006}_{-0.008}$	$0.77^{+0.02}_{-0.01}$	$0.235^{+0.005}_{-0.006}$	$2.4^{+0.4}_{-0.4}$	1,2
53721	472	G1V	5882^{+16}_{-16}	$4.31^{+0.03}_{-0.04}$	$+0.02^{+0.01}_{-0.01}$	$+0.206^{+0.021}_{-0.021}$	$6.48^{+1.44}_{-1.04}$	$1.063^{+0.022}_{-0.029}$	$1.24^{+0.04}_{-0.04}$	$0.325^{+0.028}_{-0.026}$	$2.8^{+0.2}_{-0.2}$	1,2
67275	577	F6IV	6387^{+25}_{-25}	$4.27^{+0.04}_{-0.03}$	$+0.25^{+0.02}_{-0.02}$	$+0.481^{+0.024}_{-0.024}$	$1.64^{+0.44}_{-0.52}$	$1.341^{+0.054}_{-0.039}$	$1.46^{+0.05}_{-0.05}$	$0.230^{+0.010}_{-0.005}$	$15.0^{+0.3}_{-0.3}$	1,2
96901	855	G3V	5674^{+17}_{-17}	$4.30^{+0.04}_{-0.02}$	$+0.02^{+0.01}_{-0.01}$	$+0.095^{+0.024}_{-0.024}$	$11.80^{+2.20}_{-2.00}$	$0.956^{+0.026}_{-0.025}$	$1.17^{+0.04}_{-0.03}$	$0.371^{+0.023}_{-0.024}$	$2.2^{+0.2}_{-0.2}$	1,2
100970	894	G3IV-V	5788^{+44}_{-44}	$4.18^{+0.03}_{-0.04}$	$+0.00^{+0.03}_{-0.03}$	$+0.286^{+0.069}_{-0.069}$	$9.32^{+0.76}_{-0.72}$	$1.025^{+0.020}_{-0.018}$	$1.38^{+0.06}_{-0.05}$	$0.413^{+0.026}_{-0.028}$	$2.5^{+0.5}_{-0.5}$	1,2
107350	942	G0V	5974^{+25}_{-25}	$4.48^{+0.01}_{-0.03}$	$-0.01^{+0.02}_{-0.02}$	$+0.062^{+0.033}_{-0.033}$	$0.00^{+0.88}_{-0.00}$	$1.103^{+0.012}_{-0.016}$	$1.04^{+0.02}_{-0.03}$	$0.239^{+0.010}_{-0.007}$	$10.6^{+0.3}_{-0.3}$	1,2
109378	960	G0	5555^{+44}_{-44}	$4.39^{+0.03}_{-0.03}$	$+0.20^{+0.03}_{-0.03}$	$-0.020^{+0.035}_{-0.035}$	$10.64^{+2.04}_{-2.20}$	$0.986^{+0.038}_{-0.052}$	$1.06^{+0.03}_{-0.04}$	$0.343^{+0.019}_{-0.022}$	$1.8^{+0.5}_{-0.5}$	1,2
113357	990	G2.5IVa	5787^{+25}_{-25}	$4.36^{+0.04}_{-0.03}$	$+0.15^{+0.02}_{-0.02}$	$+0.117^{+0.025}_{-0.025}$	$6.76^{+1.64}_{-1.48}$	$1.054^{+0.039}_{-0.036}$	$1.15^{+0.04}_{-0.04}$	$0.327^{+0.058}_{-0.024}$	$2.6^{+0.3}_{-0.3}$	1,2
113421	992	G8IV	5704^{+44}_{-44}	$4.42^{+0.04}_{-0.03}$	$+0.27^{+0.03}_{-0.03}$	$+0.050^{+0.031}_{-0.031}$	$5.84^{+1.92}_{-2.44}$	$1.108^{+0.034}_{-0.052}$	$1.08^{+0.04}_{-0.03}$	$0.316^{+0.022}_{-0.018}$	$0.0^{+0.5}_{-0.0}$	1,2

References: 1: Valenti & Fischer (2005), 2: Takeda et al. (2007).

Table B3. Results from the analysis of the Stokes V LSD profiles of the planet hosting stars in the BCool sample (Marsden et al. 2014, Table 3). Column 3 provides the date of the observation corresponding to the observation number shown in column 2. Column 4 shows the radial velocity for the star determined by (Marsden et al. 2014); for comparison column 5 shows the radial velocity measured by Nidever et al. (2002) (^{NS} indicates a non-radial velocity standard star; $\sigma_{res} \geq 100 \text{ m s}^{-1}$). Columns 6 and 7 show the signal-to-noise of the Stokes V profile and the number of lines used in the LSD process respectively. Column 8 indicates is the magnetic field was unambiguously detected (D), marginal (M) or not (N). Stars indicated by ⁺ have multiple observations and where appropriate the number of definite (D) and marginal (M) detections are shown as fractions of the total number of observations. HIP113357 (^{*} has multiple observations; all non-detections (N). Column 9 shows the false alarm probability calculated for the detection in column 8. Columns 10 and 11 indicate the velocity range used to calculate B_ℓ (column 12) and N_ℓ (column 13) using equation 5.

HIP no.	Obs. no.	Obs. Date	RV (this work) (km s ⁻¹)	RV (Nidever) (km s ⁻¹)	SNR _{LSD}	lines used	Detection	FAP	Velocity range (km s ⁻¹)	B_ℓ (G)	N_ℓ (G)
1499	1	19oct10	-10	-10.166	23795	11140	N	6.059×10^{-01}	-18 -2	-0.6 ± 0.5	-0.6 ± 0.5
3093 ⁺	1	10aug10	-32.7	-32.961	44842	13129	D (22/28)	$0.000 \times 10^{+00}$	-40 -25	-3.2 ± 0.2	-0.1 ± 0.2
7513	1	14nov06	-28.3	-28.674	36749	9872	N	7.340×10^{-01}	-49 -9	$+2.5 \pm 1.1$	-0.3 ± 1.1
8159	1	27jan11	-45.9	-46.022	31246	10271	N	9.024×10^{-01}	-54 -38	-0.4 ± 0.3	$+0.1 \pm 0.3$
12048	1	18dec10	-50.7	-50.971	22279	10271	N	4.743×10^{-02}	-58 -45	$+1.0 \pm 0.4$	$+0.4 \pm 0.4$
16537 ⁺	1	01feb07	16.5	16.332	39693	11754	D (52/58) M (3/58)	$0.000 \times 10^{+00}$	11 23	-10.9 ± 0.2	-0.2 ± 0.2
53721	1	31dec09	11.5	11.235	37281	9006	N	4.988×10^{-01}	5 18	$+0.6 \pm 0.2$	$+0.2 \pm 0.2$
67275 ⁺	1	13may13	-16	-16.542 ± 0.340	75344	8271	D (3/8) M (2/8)	6.090×10^{-08}	-38 5	$+3.2 \pm 0.5$	-0.1 ± 0.5
96901	1	17jul11	-27.7	-27.871	35324	9669	N	5.381×10^{-01}	-47 -9	-1.7 ± 0.9	-0.4 ± 0.9
100970	1	21jun11	-91.1	$-91.582 \pm 0.188^{\text{NS}}$	36392	10466	N	4.175×10^{-01}	-104 -77	$+1.7 \pm 0.6$	-0.6 ± 0.6
107350 ⁺	1	21jun10	-16.6	-16.833	21322	8764	D (68/91) M (7/91)	$0.000 \times 10^{+00}$	-29 -5	$+14.8 \pm 0.9$	$+0.0 \pm 0.9$
109378	1	26nov10	-20.7	-20.873	37867	12151	N	4.703×10^{-01}	-32 -9	-0.9 ± 0.5	$+0.2 \pm 0.5$
113357 [*]	1	15dec10	-33.1	-33.225	20777	11111	N	7.351×10^{-01}	-40 -27	$+0.6 \pm 0.4$	$+0.1 \pm 0.4$
113421	1	20oct10	-13.3	-13.399	21447	11135	N	5.690×10^{-01}	-31 4	-1.9 ± 1.2	-0.5 ± 1.2

Table B4. Chromospheric activity of planet-hosting stars in the BCool sample (Marsden et al. 2014, Tables 5 and 1). $B - V$ and V values are from *Hipparcos*. Where Wright et al. (2004) has calculated an S-index, this is shown in column 3. Chromospheric ages, periods and $\log(P_{rot}/\tau)$ have been determined using the equations presented in Wright et al. (2004). Sample standard deviations are used as an indication in of various errors.

HIP no.	$B - V$ (Hipparcos)	V	S-index Wright.	S-index (this work)	$\log(R'_{HK})$	Chromospheric Age (Gyr)	Chromospheric period (d)	Ca _{IRT} -index	H _α -index	$\log(P_{rot}/\tau)$
1499	0.674	6.47	0.156	0.1567 ± 0.0014	$-5.03^{+0.01}_{-0.01}$	$6.214^{+0.221}_{-0.215}$	$29.0^{+0.3}_{-0.3}$	0.7149 ± 0.0016	0.2908 ± 0.0001	$+0.336^{+0.004}_{-0.004}$
3093	0.850	5.88	0.169	0.1724 ± 0.0007	$-5.00^{+0.00}_{-0.01}$	$5.589^{+0.203}_{-0.000}$	$44.0^{+0.4}_{-0.0}$	0.7065 ± 0.0007	0.3122 ± 0.0002	$+0.324^{+0.004}_{-0.000}$
7513	0.536	4.10	0.146	0.1565 ± 0.0009	$-4.98^{+0.01}_{-0.00}$	$5.201^{+0.000}_{-0.185}$	$11.9^{+0.0}_{-0.1}$	0.7498 ± 0.0014	0.2768 ± 0.0001	$+0.316^{+0.000}_{-0.004}$
8159	0.720	6.27	0.149	0.1445 ± 0.0013	$-5.11^{+0.01}_{-0.01}$	$8.151^{+0.269}_{-0.263}$	$36.9^{+0.3}_{-0.3}$	0.6900 ± 0.0012	0.2889 ± 0.0002	$+0.366^{+0.004}_{-0.004}$
12048	0.670	6.83	0.145	0.1461 ± 0.0019	$-5.10^{+0.01}_{-0.01}$	$7.888^{+0.263}_{-0.257}$	$30.3^{+0.3}_{-0.3}$	0.7067 ± 0.0013	0.2860 ± 0.0003	$+0.362^{+0.004}_{-0.004}$
16537	0.881	3.72	0.447	0.5357 ± 0.0019	$-4.42^{+0.00}_{-0.00}$	$0.489^{+0.000}_{-0.000}$	$11.8^{+0.0}_{-0.0}$	0.8566 ± 0.0017	0.3446 ± 0.0004	$-0.262^{+0.000}_{-0.000}$
53721	0.624	5.03	0.154	0.1501 ± 0.0014	$-5.05^{+0.01}_{-0.01}$	$6.662^{+0.233}_{-0.227}$	$23.1^{+0.2}_{-0.2}$	0.7519 ± 0.0014	0.2838 ± 0.0001	$+0.343^{+0.004}_{-0.004}$
67275	0.508	4.50	0.202	0.1760 ± 0.0001	$-4.86^{+0.00}_{-0.00}$	$3.347^{+0.000}_{-0.000}$	$8.2^{+0.0}_{-0.0}$	0.7431 ± 0.0003	0.2780 ± 0.0001	$+0.259^{+0.000}_{-0.000}$
96901	0.661	6.25	0.148	0.1537 ± 0.0005	$-5.04^{+0.00}_{-0.00}$	$6.435^{+0.000}_{-0.000}$	$27.6^{+0.0}_{-0.0}$	0.7476 ± 0.0009	0.2897 ± 0.0001	$+0.340^{+0.000}_{-0.000}$
100970	0.662	6.87	0.147	0.1521 ± 0.0041	$-5.05^{+0.03}_{-0.03}$	$6.662^{+0.717}_{-0.662}$	$28.0^{+0.7}_{-0.7}$	0.7154 ± 0.0007	0.2870 ± 0.0003	$+0.343^{+0.011}_{-0.012}$
107350	0.587	5.96	-	0.3330 ± 0.0014	$-4.42^{+0.00}_{-0.00}$	$0.489^{+0.000}_{-0.000}$	$4.6^{+0.0}_{-0.0}$	0.9147 ± 0.0005	0.3153 ± 0.0003	$-0.262^{+0.000}_{-0.000}$
109378	0.773	6.54	0.155	0.1534 ± 0.0007	$-5.07^{+0.01}_{-0.00}$	$7.134^{+0.000}_{-0.239}$	$41.2^{+0.0}_{-0.4}$	0.7024 ± 0.0012	0.3000 ± 0.0002	$+0.351^{+0.000}_{-0.004}$
113357	0.666	5.45	0.148	0.1528 ± 0.0021	$-5.06^{+0.01}_{-0.02}$	$6.895^{+0.484}_{-0.233}$	$28.7^{+0.5}_{-0.3}$	0.7154 ± 0.0014	0.2900 ± 0.0002	$+0.347^{+0.008}_{-0.004}$
113421	0.744	6.17	0.15	0.1494 ± 0.0029	$-5.09^{+0.02}_{-0.02}$	$7.630^{+0.521}_{-0.496}$	$39.0^{+0.7}_{-0.7}$	0.6861 ± 0.0006	0.2979 ± 0.0003	$+0.359^{+0.008}_{-0.008}$